and silver as-
002ϕ_1. Com-

in α-iron has
se data to es-
grain bound-

er and that a
positions will

orus segrega-
sition, calcu-

14

STRUCTURE AND ENERGY OF HETEROPHASE INTERFACES

In Section 13.2, we focused our attention on homophase interfaces, where there was a structural discontinuity between two crystals of the same phase, as illustrated in Figures 12.1 and 12.2, for example. In Section 13.2.5, we calculated the interfacial energy of an f.c.c.–h.c.p. interface (Fig. 12.4), because it followed directly from calculation of the stacking fault and twin boundary energies in that section. However, the f.c.c.–h.c.p. interface is actually a heterophase interface, because the two phases on opposite sides of the interface have different crystal structures. This represents one limiting type of heterophase boundary at which there is a change in Bravais lattice, but no change in composition across the interface. In this chapter, we examine the structure and properties of the other types of heterophase interfaces that show a change in composition or both composition and lattice across the interface between two different phases. We begin by examining a planar, fully coherent interface between two different phases that have the same Bravais lattice and orientation, but differ in composition. An example of this is illustrated by the G.P. zone in Figure 12.3. In our treatment of this situation, we will derive a series of equations based on a nearest-neighbor broken bond (regular solution) model to calculate the composition profiles across the various interfaces of the aluminum–silver G.P. zone in Figure 12.3. We then combine our approaches to quantifying structural and compositional changes across an interface to treat semicoherent and inclined interfaces such as those shown in, for example, Figures 12.5 and 12.7. Next we look at other properties of heterophase interfaces, such as their roughening, kinetic and segregation behavior, for comparison with the same properties discussed previously for solid–vapor, solid–liquid and homophase solid–solid interfaces.

14.1. INTERPHASE BOUNDARY ENERGY

In principle, it is possible to determine the interphase boundary energy between two solid phases by (a) the thermal grooving technique, (b) measuring contact angles, (c) performing nearest-neighbor bond-breaking or atomistic calculations, and (d) measuring the coarsening behavior of coherent precipitates; all of these methods have been utilized [24]. Unfortunately, in many of the experimental data reported in the literature, there is considerable uncertainty in the values of the interfacial energy because the orientation relationship between the two phases and the structure of the interface were not determined. This uncertainty arises because the interfacial energy of a heterophase interface depends on the orientation relationship and atomic matching at the interface in much the same way as the grain boundary energy in Section 13.2 depended on whether the boundary was a low- or high-angle tilt or twist boundary. In addition, some measurements were not obtained under carefully controlled conditions, and surface contamination may have affected the results.

In spite of the rather large uncertainty often associated with measurement of the interphase boundary energy in any one investigation, there have been enough measurements made on various types of heterophase interfaces that it is possible to assign a reasonable range of values for the interfacial energies of the three main types of planar heterophase interfaces. Although tables of interfacial energies were provided for the solid–vapor, solid–liquid and homophase interfaces discussed previously, here we provide only ranges for various heterophase interfaces because of the uncertainties just mentioned. The ranges provided in Table 14.1 correspond to coherent interfaces as in Figures 12.3 and 12.4, to semicoherent interfaces as in Figure 12.5, and to incoherent interfaces, as in Figure 12.6.

There have not been any accurate experimental determinations of the interfacial energy of a stepped heterophase interface such as that shown in Figure 12.7. The elastic strain energy associated with such an interface has been calculated [56], and, in principle, it can be added to the compositional component of the interfacial energy to obtain an estimate of the interphase boundary energy, as described in Section 14.5.4. Recent atomistic calculations have been performed to determine the interfacial energies of ledged f.c.c.–b.c.c. interfaces in iron and nickel–chromium alloys [100–102]. Values obtained in these studies indicate that the interfacial energies of coherent, stepped interfaces should lie in the lower end of the range for a semicoherent interface given in Table 14.1.

Table 14.1. Ranges of solid–solid interphase boundary energies γ^{SS} for three types of planar interfaces

Interface	γ^{SS} (mJ/m^2)
Coherent	5–200
Semicoherent	200–800
Incoherent	800–2500

between two
ontact angles,
tions, and (d)
hese methods
ita reported in
rfacial energy
ructure of the
rfacial energy
p and atomic
ary energy in
h-angle tilt or
nder carefully
e results.
easurement of
been enough
is possible to
he three main
energies were
discussed pre-
es because of
correspond to
aces as in Fig-

of the interfa-
Figure 12.7.
alculated [56],
the interfacial
cribed in Sec-
ermine the in-
chromium al-
he interfacial
the range for a

14.2. COHERENT INTERPHASE BOUNDARY STRUCTURE AND ENERGY

The treatments discussed in this section apply to the special case of two phases with the same crystal structure but different compositions. Three treatments of this type of interface are described, two of which are based on our familiar broken-bond model and the third uses a continuum approach to the problem. These theories are described in chronological order, which is convenient in the development of this chapter.

14.2.1. Becker Model

The simplest and earliest calculation of the interfacial energy of a fully coherent interface between two phases α and β that differ in composition was done by Becker [103]. He employed a nearest-neighbor broken-bond model to derive the coherent solid–solid interphase boundary energy γ_c^{SS}, assuming that both phases are homogeneous up to the interface, as illustrated in Figure 14.1. The energy is given as

$$\gamma_c^{SS} = N_{s\{hkl\}} z_j (X_\alpha - X_\beta)^2 \epsilon, \tag{14.1}$$

where $N_{s\{hkl\}}$ is the number of atoms per unit area on the $\{hkl\}$ interface plane, z_j is the coordination number across the interface, X_α and X_β are the equilibrium atom fractions of solute B in the α and β phases, respectively, and ϵ is defined according to the regular solution model in Eq. (2.19).

To illustrate the use of Eq. (14.1), consider the gold–nickel system shown in Problem 2.11. This alloy possesses a miscibility gap with a critical temperature $T_c = 810.3℃$ and composition $X_B^c = 0.706$. Suppose we want to calculate the energy of a coherent $\{111\}$ interphase boundary at 400℃. From the phase diagram, $X_\alpha = 0.075$ and $X_\beta = 0.985$ at 400℃ so that $(X_\alpha - X_\beta)^2 = 0.828$. The lattice parameter of gold is 0.40 nm, so $N_{s\{111\}} = 4/\sqrt{3}(0.4\times10^{-9}\text{ nm})^2 = 1.44\times10^{19}$ atoms/m² and $z_j = 3$ for the $\{111\}$ plane. We can find Ω (and thus ϵ) from T_c and X_B^c using Eq. (2.27) as $\Omega = (8.315\text{ J/mol·K})(1083.3\text{ K})/2(0.706)(0.295) = 21{,}695$ J/mol. Since $\epsilon = \Omega/12N_A$ (Eq. 2.22),

$$\gamma^{SS}_{c(\text{Au–Ni})} = \frac{(1.44\times10^{19}\text{ atoms/m}^2)3(0.828)(21{,}695\text{ J/mol})}{12(6.022\times10^{23}\text{/mol})} = 0.107\text{ J/m}^2.$$

This is a fairly high value for a coherent interphase boundary energy, mainly due to the high positive enthalpy of mixing in the gold–nickel system.

The main limitation of Eq. (14.1) is that it assumes that the boundary is infinitely sharp, as illustrated in Figure 14.1, and does not include the interphase boundary width as a thermodynamic variable. The gradient energy theory and discrete lattice plane models that follow show that this assumption is only valid for alloys with a large positive enthalpy of mixing ($\Omega > 0$) at 0 K. Thus, although this equation is appealingly simple and it can be used to obtain an estimate of the inter-

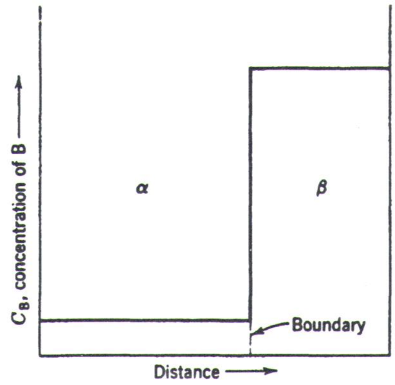

Figure 14.1. Illustration of composition versus distance across an ideal planar boundary between the α and β phases. From [104] reprinted by permission of John Wiley & Sons, Inc.

phase boundary energy, it does not properly describe the underlying physics associated with many interphase boundaries.

14.2.2. Cahn–Hilliard (Gradient Energy) Model

Cahn and Hilliard [10] developed a continuum description of the coherent interphase boundary energy by considering a flat interface of area A between two isotropic phases α and β of composition C_α and C_β and assuming that the free energy of nonequilibrium material of composition intermediate between C_α and C_β can be represented by a continuous free-energy function $G_0(C)$ as shown in Figure 14.2. The function $G_0(C)$ is identical to G^s in Figures 2.8 and 2.9, for example. They express the total free energy G of the solution as a multivariable Taylor's series expansion about G_0, the free energy per molecule of a solution of uniform composition C. By considering only a one-dimensional composition change across the interface and neglecting derivative terms higher than the second, they obtained

$$G = AN_v \int_{-\infty}^{+\infty} [G_0(C) + \kappa(dC/dx)^2]\, dx, \qquad (14.2)$$

where N_v is the number of molecules per unit volume and

$$\kappa = -[\partial^2 G/\partial C \partial \nabla^2 C]_0 + [\partial^2 G/(\partial|\nabla C|)^2]_0. \qquad (14.3)$$

Equation (14.2) indicates that to first approximation, the free energy of a small volume of nonuniform solution can be expressed as the sum of two contributions, one being the free energy that this volume would have in a homogeneous solution ($G_0(C)$) and the other being a gradient energy contribution ($\kappa(dC/dx)^2$), which is a function of the local composition.

The specific interfacial free energy γ_c^{SS} is, by definition, the difference per unit area between the actual free energy of the system and that which it would have if the properties of the phases were continuous throughout; thus, it can be written as

---

Figure 14.2.
mission from
of John Wiley

where

and μ_A^e and
or β phases
free energy
tion C_α or
fuse the inte
$\kappa(dC/dx)^2$ t
ducing more
expense of
tion variable
alent to the
tem.)

To ob
for γ_c^{SS}, the

ır boundary be-
ι Sons, Inc.

ıhysics associ-

oherent inter-
between two
the free ener-
C_α and C_β can
n Figure 14.2.
nple. They ex-
series expan-
omposition C.
interface and

(14.2)

(14.3)

of a small vol-
ributions, one
eous solution
$)^2$), which is a

difference per
it would have
n be written as

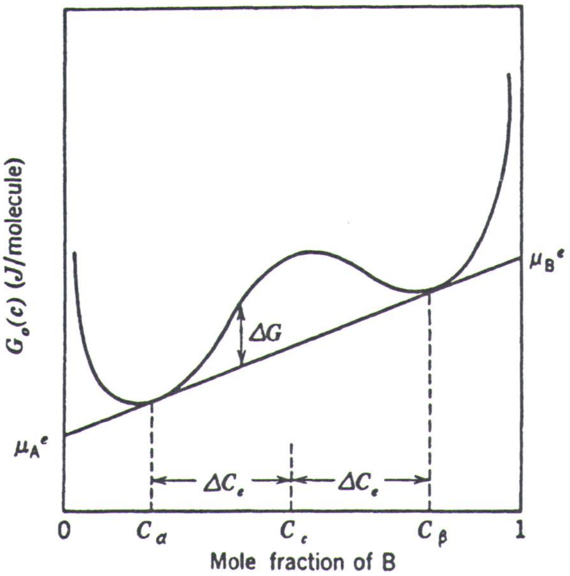

Figure 14.2. The function $G_0(C)$ for T less than the critical temperature T_c. Reprinted with permission from [10] by Elsevier Science Ltd., Oxford, England and [104] reprinted by permission of John Wiley & Sons, Inc.

$$\gamma_c^{SS} = N_v \int_{-\infty}^{+\infty} [\Delta G(C) + \kappa (dC/dx)^2]\, dx, \tag{14.4}$$

where

$$\Delta G(C) = G_0(C) - [C\mu_B^e + (1 - C)\mu_A^e] \tag{14.5}$$

and μ_A^e and μ_B^e are the chemical potentials per atom of the species A and B in the α or β phases at equilibrium. The quantity $\Delta G(C)$ may therefore be referred to as the free energy per atom of transferring material from an infinite reservoir of composition C_α or C_β to material of composition C. According to Eq. (14.4), the more diffuse the interface is, the smaller the contribution will be of the gradient energy term $\kappa(dC/dx)^2$ to γ_c^{SS}. However, this decrease in energy can only be achieved by introducing more material of nonequilibrium composition at the interface and thus at the expense of increasing the integrated value of $\Delta G(C)$. At equilibrium, the composition variable will be such as to minimize the integral of this equation. (This is equivalent to the requirement that the chemical potentials be constant throughout the system.)

To obtain a composition profile with a stationary value and a minimum value for γ_c^{SS}, the following condition must hold

$$\Delta G(C) = \kappa (dC/dx)^2. \tag{14.6}$$

Changing the variable of integration from x to C and substituting Eq. (14.6) into Eq. (14.4) then yields

$$\gamma_{\mathrm{c}}^{\mathrm{SS}} = 2N_{\mathrm{v}} \int_{C_\alpha}^{C_\beta} [\kappa \Delta G(C)]^{1/2}\, \mathrm{d}C. \tag{14.7}$$

Cahn and Hilliard [10] examine Eq. (14.7) in two forms: (a) to determine the functional dependence of $\gamma_{\mathrm{c}}^{\mathrm{SS}}$ on temperature in the immediate vicinity of the critical temperature T_{c} at which the two phases attain the same critical composition C_{c}, and (b) to determine the absolute value of $\gamma_{\mathrm{c}}^{\mathrm{SS}}$ and its temperature dependence outside the range $T \sim T_{\mathrm{c}}$ by using a regular solution model to evaluate the gradient term κ and the free energy function $\Delta G(C)$.

In the first case, if G_0 is expanded in a Taylor's series about C_0, and κ is assumed to be continuous and nonvanishing in the vicinity of the critical point, the interfacial energy is evaluated as

$$\gamma_{\mathrm{c}(T\sim T_{\mathrm{c}})}^{\mathrm{SS}} = (2\sqrt{2}N_{\mathrm{v}}/3\mathfrak{B})\kappa^{1/2}\mathfrak{x}^{3/2}(T_{\mathrm{c}} - T)^{3/2}, \tag{14.8}$$

where $\mathfrak{B}$ and $\mathfrak{x}$ are inherently positive constants defined by the following derivatives of G_0 evaluated at $C = C_{\mathrm{c}}$ and $T = T_{\mathrm{c}}$,

$$\mathfrak{B} = (\partial^4 G_0/\partial C^4)/4! \tag{14.9a}$$

$$\mathfrak{x} = (\partial^3 G_0/\partial T \partial C^2)/2!. \tag{14.9b}$$

Therefore, at the critical temperature, the interfacial energy is proportional to $(T_{\mathrm{c}} - T)^{3/2}$.

Furthermore, if the composition across the interface is such that $\mathrm{d}C/\mathrm{d}x = (\Delta G/\kappa)^{1/2}$, then inspection of the ΔG function in Figure 14.2 indicates that to satisfy this equation the composition profile must be sigmoidal in shape, as shown in Figure 14.3. Near the critical temperature, the thickness L of the interface is obtained as

$$L_{(T\sim T_{\mathrm{c}})} = 2[2\kappa/\mathfrak{x}(T_{\mathrm{c}} - T)]^{1/2} \tag{14.10}$$

and it becomes evident that the thickness of the interface increases with increasing temperature and becomes infinite at the critical temperature. Qualitatively, this is the same type of behavior depicted schematically in Figure 3.3. Note that this treatment assumes that κ is a positive quantity.

In the second case, if the following properties of a regular (R) solution (refer to Sections 2.4 and 2.5) are used:

$$C_{\mathrm{c}} = 0.5 \tag{14.11a}$$

$$\mu_A = \Omega C^2 - k_{\mathrm{B}} T \ln(1 - C) \tag{14.11b}$$

q. (14.6) into Eq.

(14.7)

termine the func-
ity of the critical
mposition C_c, and
pendence outside
e gradient term κ

it C_0, and κ is as-
tical point, the in-

(14.8)

owing derivatives

(14.9a)

(14.9b)

s proportional to

uch that dC/dx =
ates that to satisfy
, as shown in Fig-
face is obtained as

(14.10)

es with increasing
alitatively, this is
ote that this treat-

R) solution (refer

(14.11a)

(14.11b)

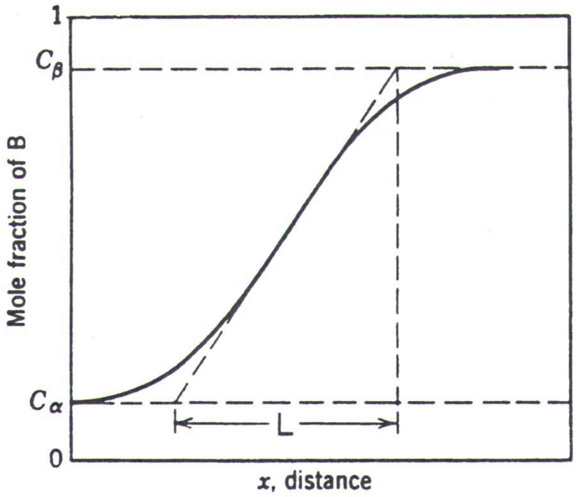

Figure 14.3. Composition of α and β in the vicinity of the interphase boundary. Note the difference between this profile and that shown in Figure 14.1. Reprinted with permission from [10] by Elsevier Science Ltd., Oxford, England and [104] reprinted by permission of John Wiley & Sons, Inc.

$$\Omega = 2k_BT_c \tag{14.11c}$$

$$\ln \frac{C_e}{1 - C_e} = (2C_e - 1)\frac{\Omega}{k_BT}, \tag{14.11d}$$

then an expression for the free energy referred to a standard state of an equilibrium mixture of α and β becomes

$$\Delta G_R = G_R(C) - G_R(C_e) \tag{14.12a}$$

$$= \Omega(C - C_e)^2 + k_BT\left[C \ln \frac{C}{C_e} + (1 - C)\ln \frac{1 - C}{1 - C_e}\right], \tag{14.12b}$$

in which C_e can be set equal to either of the compositions C_α or C_β as indicated in Figure 14.2, and Ω is the regular solution parameter (Eq. 2.22). If Eq. (14.12b) is differentiated and the values for $\mathfrak{z}$ and $\mathfrak{x}$ in Eqs. (14.9) are substituted, it is found that

$$\mathfrak{x}_R = 2k_B \tag{14.13a}$$

$$\mathfrak{z}_R = \frac{4k_BT_c}{3}. \tag{14.13b}$$

These parameters can then be substituted into the general equation for the interfacial free energy giving

$$\gamma_{\mathrm{cR}}^{\mathrm{SS}} = 2N_v x_{\mathrm{R}} k_{\mathrm{B}} T_{\mathrm{c}} \gamma_{\mathrm{cr}}^{\mathrm{SS}}, \tag{14.14}$$

where $\gamma_{\mathrm{cr}}^{\mathrm{SS}}$ is a reduced interfacial energy defined by

$$\gamma_{\mathrm{cr}}^{\mathrm{SS}} = \int_{C_\alpha}^{C_\beta} \left(\frac{\Delta G_{\mathrm{R}}}{k_{\mathrm{B}} T_{\mathrm{c}}} \right)^{1/2} \mathrm{d}C \tag{14.15}$$

and the parameter x_{R} has the dimensions of length and represents a root-mean-square effective interaction distance for the energy in a concentration gradient. The parameter x_{R} is very sensitive to the exact nature of long-range molecular interactions and can vary from $r_e/\sqrt{3}$, where r_e is the interatomic distance, for a simple nearest-neighbor interaction, to a value of $(11/7)^{1/2} r_e$ for a 6–12 potential.

The integral in Eq. (14.15) has been evaluated numerically and is plotted in Figure 14.4a as $\gamma_{\mathrm{cr}}^{\mathrm{SS}}$ versus T/T_{c} and in Figure 14.4b as $\log(\gamma_{\mathrm{cr}}^{\mathrm{SS}})$ versus $\log(1 - T/T_{\mathrm{c}})$. An approximate expression for $\gamma_{\mathrm{cR}}^{\mathrm{SS}}$ that is valid over the whole temperature range was obtained from these data and is given by

$$\gamma_{\mathrm{cR}}^{\mathrm{SS}} \sim 2N_v x_{\mathrm{R}} (k_{\mathrm{B}} T_{\mathrm{c}})^{1/2} \left[\frac{\pi \Delta C_e (\Delta G_{\mathrm{R}}^{\max})^{1/2}}{2} \right] \left[1 - \left(\frac{\pi}{2} - \frac{4}{3} \right) \left(\frac{T}{T_{\mathrm{c}}} \right) \right], \tag{14.16a}$$

where

$$\Delta G_{\mathrm{R}}^{\max} = -2k_{\mathrm{B}} T_{\mathrm{c}} (C_{\mathrm{c}} - C_\alpha)^2 + k_{\mathrm{B}} T \left[C_{\mathrm{c}} \ln \frac{C_{\mathrm{c}}}{C_\alpha} + (1 - C_{\mathrm{c}}) \ln \frac{1 - C_{\mathrm{c}}}{1 - C_\alpha} \right] \tag{14.16b}$$

$$\Delta C_e = (C_{\mathrm{c}} - C_\alpha) \tag{14.16c}$$

and C_{c} is the critical composition. In the case of a symmetric miscibility gap, $C_{\mathrm{c}} = 0.5$, as shown in Figure 14.2. This equation can be used with Eq. (14.11d) to calculate $\gamma_{\mathrm{cR}}^{\mathrm{SS}}$ with an error of less than one percent. As in the previous case, the interface thickness can be defined in the case of a regular solution model and is given by

$$\frac{L_{\mathrm{R}}}{x_{\mathrm{R}}} = \sqrt{2} \left\{ -1 - \frac{T \ln 4C_e(1 - C_e)}{[T_{\mathrm{c}}(1 - 2C_e)^2]^{-1/2}} \right\} \tag{14.17}$$

For a regular solution the interface profile is symmetric about $C = 0.5$ (Fig. 14.3). This quantity has been calculated numerically and is plotted versus T/T_{c} in Figure 14.5. When $T \sim T_{\mathrm{c}}$ an equation similar to Eq. (14.10) results for the regular solution model as

$$\frac{L_{\mathrm{R}}}{x_{\mathrm{R}}}(T \sim T_{\mathrm{c}}) = 2 \left[\frac{T_{\mathrm{c}}}{(T_{\mathrm{c}} - T)} \right]^{1/2}. \tag{14.18}$$

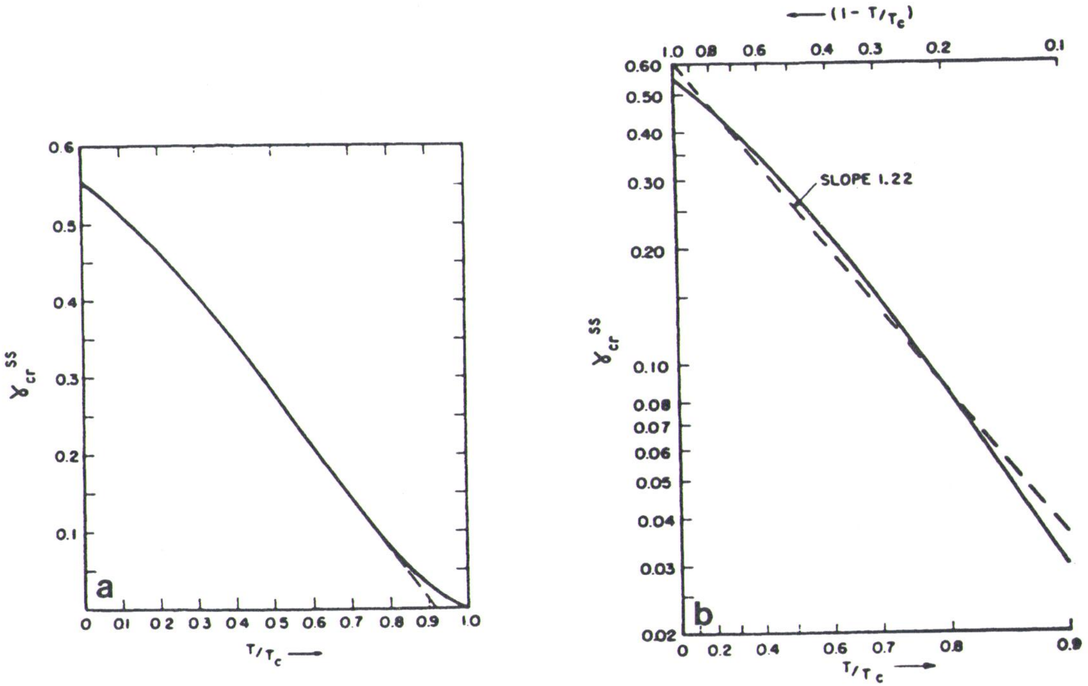

Figure 14.4. Reduced interfacial free energy γ_{cr}^{SS} versus T/T_c for a regular solution plotted on (a) linear and (b) logarithmic scales. Reprinted with permission from [10] by Elsevier Science Ltd., Oxford, England.

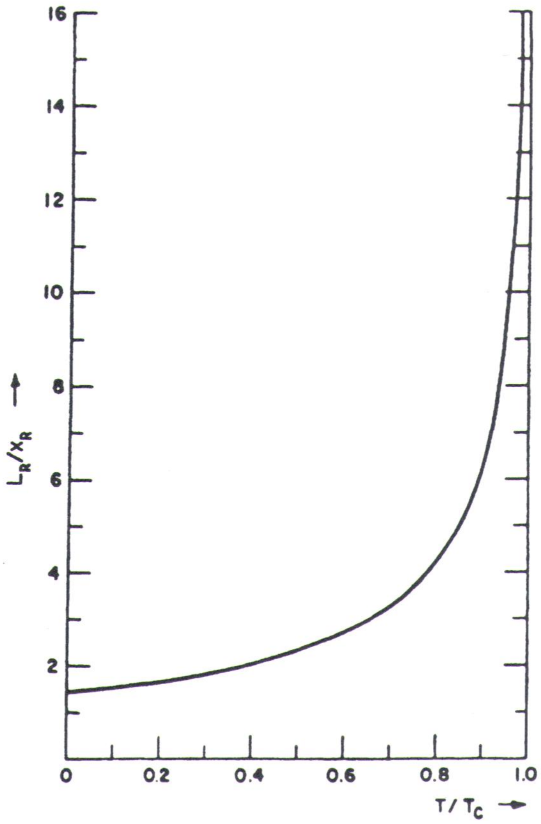

Figure 14.5. Plot of interfacial width L_R/x_R versus T/T_c for a regular solution. Reprinted with permission from [10] by Elsevier Science Ltd., Oxford, England.

An empirical expression for the temperature dependence of the liquid–vapor interfacial energy was given in Eq. (3.16) in Section 3.1, where it was indicated that a value of $n = 1.2$ fitted the behavior of many substances. This equation with a value of $n = 1.22$ is plotted as a dashed line in Figure 14.4b, where it is seen that Eq. (3.16) agrees with the temperature dependence of the interfacial energy from the Cahn–Hilliard theory to within a few percent over a major portion of the temperature range. This shows a striking similarity in the behavior of the interfacial energies of liquid–vapor and coherent solid–solid interfaces.

14.2.3. Discrete Lattice Plane Model

More recently, Lee and Aaronson [105] developed a discrete lattice plane (DLP), regular solution model to calculate the interphase boundary energy and interfacial concentration profiles across coherent interphase boundaries. Although the DLP model was originally developed by Wynblatt and Ku [106] to analyze surface segregation, these two processes are physically analogous, because the movement of atoms to or away from a coherent interface in an attempt to reach an equilibrium state is similar to segregation to a surface that is initially not in an equilibrium configuration. The problem is thus reduced to calculating ΔH and ΔS, the enthalpy and entropy changes accompanying the net atomic movements required to reach the equilibrium configuration of the α and β phases from an initial state. The homogeneous α phase is taken as the initial or reference state in this treatment for convenience.

In this model, the system is assumed to consist of n solute (B) atoms in N atomic sites. When equilibrium is achieved throughout the system, the ith layer of the boundary region parallel to the interface plane contains n_i of B atoms per unit area at the interface $N_{s\{hkl\}}$, such that X_i is the atom fraction of B in the ith boundary layer, as illustrated in Figure 14.6. This figure also shows how the nearest-neighbor atoms are distributed around an atom P on the ith boundary plane, where z_l is the lateral coordination number and z_j is the coordination number to the nearest neighboring atoms in the j plane, as in Eq. (6.30). The total coordination number z is thus,

$$z = z_l + 2\sum z_j. \tag{14.19}$$

The average bond enthalpy change attending the breaking of bonds between a B atom in the bulk α phase with composition X_α and its nearest neighbors and the

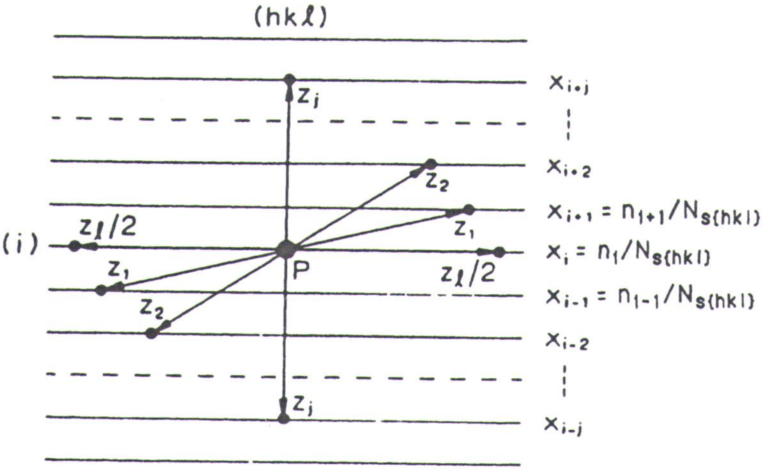

Figure 14.6. Diagram showing the distribution of z nearest neighbors about atom P in adjacent planes parallel to (hkl). z_j is the unidirectional vertical coordination number to the jth plane as determined from the plane i. Reprinted with permission from [105] by Elsevier Science Ltd., Oxford, England.

forming of bonds between this atom and its nearest neighbors in the *i*th boundary layer is

$$\frac{1}{2}\{\sum_j (X_{i+j} + X_{i-j})z_j + X_i z_1 - X_\alpha z\}(\epsilon_{BB} - \epsilon_{AB}) \tag{14.20a}$$

and a similar expression can be written for the bond enthalpy change undergone by an *A* atom displaced from the *i*th α boundary plane to the bulk as

$$\frac{1}{2}\{\sum_j (X_{i+j} + X_{i-j})z_j + X_i z_1 - X_\alpha z\}(\epsilon_{AB} - \epsilon_{AA}). \tag{14.20b}$$

The sum of Eqs. (14.20a and b) represents the enthalpy change associated with the segregation of a *B* atom to the *i*th boundary plane Δh_i, that is,

$$\Delta h_i = \epsilon\{X_\alpha z - X_i z_1 - \sum_j (X_{i+j} + X_{i-j})z_j\}, \tag{14.21}$$

where $\epsilon = \epsilon_{AB} - 1/2(\epsilon_{AA} + \epsilon_{BB})$ and the total bond enthalpy required to reach the equilibrium state from the reference state is, thus,

$$\Delta H = N_{s\{hkl\}} \sum_i (X_i - X_\alpha)\Delta h_i, \tag{14.22}$$

where the sum is used to denote summation over the entire boundary region. The binding enthalpies are dependent on orientation through z_j and z_1 in Eq. (14.21).

The entropy change attending segregation to the boundary is due to the configurational entropy difference between the equilibrium state and the reference state [105] and is given by

$$\Delta S = -N_{s\{hkl\}} k_B \sum_i \left[X_i \ln\frac{X_i}{X_\alpha} + (1 - X_i)\ln\frac{1 - X_i}{1 - X_\alpha}\right]. \tag{14.23}$$

The equilibrium solute distribution in the boundary region is achieved when

$$\frac{\partial(\Delta G)}{\partial X_i} = 0, \tag{14.24}$$

where

$$\Delta G = \Delta H - T\Delta S \tag{14.25}$$

and Eq. (14.22) is substituted for ΔH and Eq. (14.23) for ΔS. Equation (14.24) then yields a series of difference equations that must be solved simultaneously for X_i according to

$$2\epsilon\{X_\alpha z - X_i z_1 - \sum_j (X_{i+j} + X_{i-j})z_j\} - k_B T\left\{\ln\frac{1}{X_i - 1} - \ln\frac{1}{X_\alpha - 1}\right\} = 0. \tag{14.26}$$

The summation is performed over all boundary planes whose composition differs significantly from either X_α or $(1 - X_\alpha)$ and a computer is used to evaluate the X_i from this equation.

As in the previous Cahn–Hilliard analysis [10], the interfacial energy is defined as the free energy difference between an equilibrated mixture of α and β, and homogeneous α and β of equilibrium composition which are continuous up to the interface. When ΔH and ΔS are substituted into Eq. (14.25) for the total free energy ΔG above and appropriate mathematical rearrangements are performed [105], the coherent boundary energy becomes

$$\gamma_{\mathrm{c}}^{\mathrm{SS}} = N_{\mathrm{s}\{hkl\}} \sum_i \Bigg\{ -\epsilon (X_i - X_\alpha)^2 z + \epsilon \sum_j (X_i - X_{i+j})^2 z_j + k_{\mathrm{B}}T\left[X_i \ln \frac{X_i}{X_\alpha} + (1 - X_i) \ln \frac{1 - X_i}{1 - X_\alpha}\right]\Bigg\}. \tag{14.27}$$

When $T = 0$ K, Eq. (14.27) is simplified by noting that the interface is no longer diffuse, since both X_α and the $k_{\mathrm{B}}T$ terms become equal to zero and thus so must all the values for X_i in the α phase. Similarly, when the β phase is considered, X_α and all the values of X_i are replaced by $-X_\beta$ and $-X_j$, and these terms must be unity at 0 K. Hence, the concentration difference across the interface jumps directly from zero to unity and the only remaining term in Eq. (14.27) at $T = 0$ K is

$$\gamma_{\mathrm{c}}^{\mathrm{SS}} = N_{\mathrm{s}\{hkl\}} \epsilon \sum_j (X_i - X_{i+j})^2 z_j. \tag{14.28a}$$

Note that this is the same as Eq. (14.1). Under this condition, when both planes i and $(i+j)$ are in the same phase, $(X_i - X_{i+j})^2 = 0$ and, when i is in the α phase and plane $(i+j)$ is in the β phase, $(X_i - X_{i+j})^2 = 1$. Thus Eq. (14.28a) reduces to

$$\gamma_{\mathrm{c}}^{\mathrm{SS}} = N_{\mathrm{s}\{hkl\}} \epsilon \sum_j z_j \tag{14.28b}$$

and $\gamma_{\mathrm{c}}^{\mathrm{SS}}$ at 0 K is simply proportional to the number of broken bonds when the interphase boundary is ruptured exactly along the interface. This is similar to the Becker model in the limit of no solubility, which yields results that are similar to the treatment of the surface energy in Part II and we therefore expect a similar anisotropy of the coherent interphase boundary energy as a function of orientation.

To investigate the orientation dependence of $\gamma_{\mathrm{c}}^{\mathrm{SS}}$ and the resulting concentration profile, it is necessary to evaluate $N_{\mathrm{s}\{hkl\}}$, z_1 and z_j as a function of orientation for a particular value of ϵ. This was performed for an f.c.c. crystal system using a regular solution model with $\epsilon = 0.167 k_{\mathrm{B}} T_{\mathrm{c}}$, where the calculations can be confined to within the unit stereographic triangle due to symmetry, as for the previous solid–vapor surfaces. The procedure for evaluating these quantities is similar to that discussed with regard to Eq. (3.20) and the reader is referred to the original references for further details [105,107].

Figure 14.7 shows the concentration profiles in one phase at three temperatures for the (100), (110) and (111) planes only. The profiles for the other half of these interfaces is an inverted mirror image of those shown in this figure because of the symmetry relation across the interface (refer to Fig. 14.3). The profiles are given in units of the lattice parameter of the f.c.c. phase α . Note that the concentration profile is controlled solely by T/T_c and is independent of boundary orientation above about $0.6T/T_c$, in agreement with the previous results of Cahn and Hilliard [10]. This situations applies at a relatively high value of T/T_c when the concentration gradient is small across the boundary zone. Comparing the curves for $0.5T/T_c$ in Figure 14.7 shows that there is some difference between the two treatments at $0.5T/T_c$ when the concentration gradient is relatively steep. The concentration profiles in Figure 14.7 would continue to flatten as the temperature is raised until T_c, where the plot would appear as a horizontal line at $X_i = 0.5$, as in Figure 3.3.

At $T = 0$ K, Eq. (14.28) yields γ_c^{SS} directly by summing over the planes j. At higher temperatures, Eq. (14.26) must be solved for X_i for various (hkl) planes and the results incorporated into Eq. (14.27). The resulting calculations for γ_c^{SS} are shown in the form of contour plots in the stereographic triangle in Figure 14.8 for $T/T_c = 0$, 0.25 and 0.5, respectively. These results are normalized to unity at (100) and the result for 0 K in Figure 14.8a is similar to that for the surface energy of a pure f.c.c. crystal shown previously in Figure 3.10. As T increases in Figures 14.8b and c, γ_c^{SS} is not a simple function of the number of bonds across the interface and the energy contours do not consist of spheres centered about (210) as in Figure

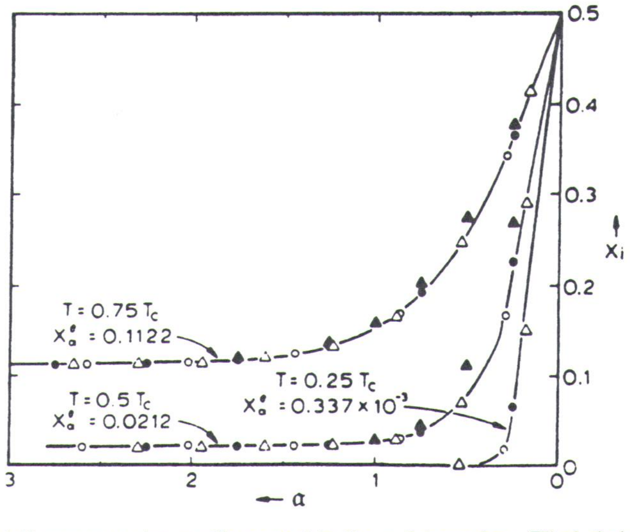

Figure 14.7. Half concentration profile normal to the α–β boundary. Filled circles represent (100), open circles (111), open triangles (110) and filled triangles are from the Cahn–Hilliard (continuum) analysis. Reprinted with permission from [105] by Elsevier Science Ltd., Oxford, England.

t three tempera-
he other half of
igure because of
rofiles are given
e concentration
dary orientation
hn and Hilliard
e concentration
s for $0.5T/T_c$ in
o treatments at
ncentration pro-
raised until T_c,
gure 3.3.
the planes *j*. At
(*hkl*) planes and
ons for γ_c^{SS} are
Figure 14.8 for
o unity at (100)
face energy of a
in Figures 14.8b
he interface and
0) as in Figure

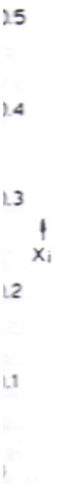

circles represent
the Cahn–Hilliard
ence Ltd., Oxford,

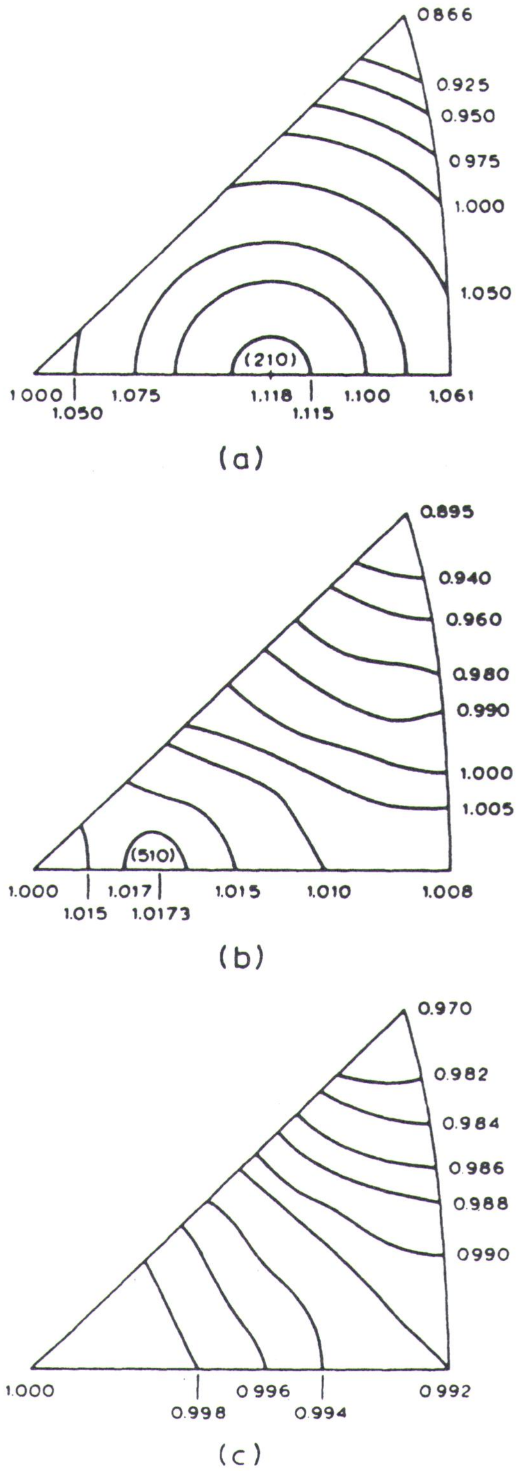

Figure 14.8. γ_c^{SS} plots for (a) 0 K, (b) $0.25T_c$ and (c) $0.5T_c$. The results are normalized to unity at (100). Reprinted with permission from [105] by Elsevier Science Ltd., Oxford, England.

14.8a. In addition, the degree of anisotropy decreases with temperature from approximately 1.30 at 0 K, 1.14 at $0.25T_c$, 1.03 at $0.5T_c$ and to less than 1.006 at $0.75T_c$ (not shown). These results are similar to those for the surface energy of copper versus temperature shown in Figure 3.11 and for lead in Figure 3.16. Such a small anisotropy at $0.75T_c$ indicates that, at higher temperatures, γ_c^{SS} is effectively orientation independent. Note that a cusp exists at (111) for all of the temperatures investigated, and that the maximum energy moves from (210) toward (100) such that the maximum occurs at (100) at and above $0.5T_c$. This is an unexpected result, because most experimental studies of the surface energy show that the maximum surface energy is located at approximately the center of the unit triangle.

Lee and Aaronson [105] have shown that the discrete lattice plane formalism can be used to derive the regular solution version of the Cahn–Hilliard (CH) continuum equation for γ_c^{SS} and they compare the CH theory (curve c), discrete lattice plane (DLP) model (curves a and b) and Becker theory (curve d) in Figure 14.9 for the (111) and (100) interfaces. Above about $0.7T_c$, the CH and DLP theories con-

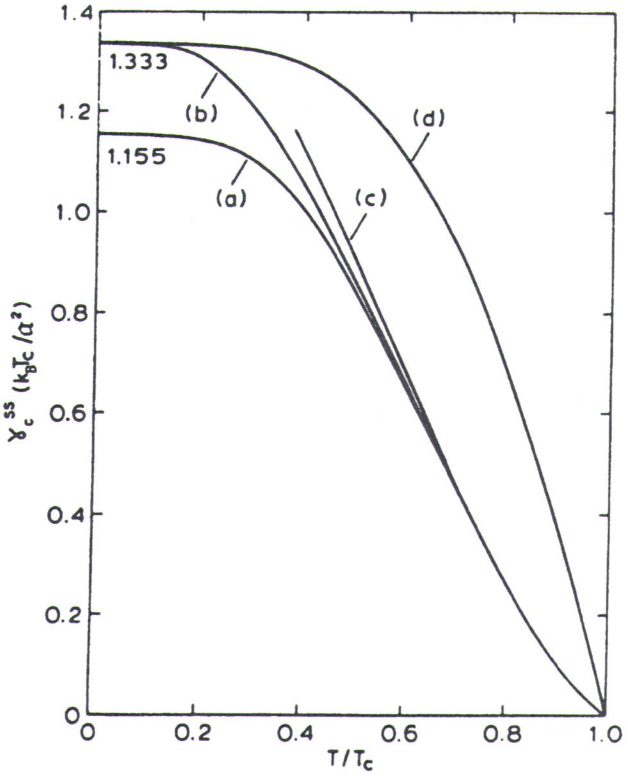

Figure 14.9. Comparison of the values of γ_c^{SS} in an f.c.c. crystal. Curves (a) and (b) are for (111) and (100) from the DLP model, curve (c) is from Eq. (14.16) and curve (d) is for Eq. (14.1). Reprinted with permission from [105] by Elsevier Science Ltd., Oxford, England.

---

verge, which
ture of γ_c^{SS}
theories with
reduction in
that Becker's

Lee an
nents to the
two compon
sent the free
solute conce
X_α, and (b)
concentration
For a solid s
gap, both ter
two terms to
where the fir
is identified
is maximum
decreases ste

Figure 14.10.
Reprinted with

mperature from ap-
less than 1.006 at
rface energy of cop-
Figure 3.16. Such a
s, γ_c^{SS} is effectively
of the temperatures
toward (100) such
n unexpected result,
that the maximum
triangle.
ice plane formalism
Hilliard (CH) contin-
e c), discrete lattice
d) in Figure 14.9 for
DLP theories con-

ves (a) and (b) are for
ve (d) is for Eq. (14.1).
England.

verge, which supports the equivalency of these models as well as the isotropic nature of γ_c^{SS} at high temperatures. Comparison of the CH and DLP diffuse interface theories with Becker's result for an abrupt (100) interface shows that a significant reduction in surface energy occurs as an interface becomes diffuse and, therefore, that Becker's result is only valid for $T < 0.2T_c$.

Lee and Aaronson [105] also compared the contributions of the two components to the interfacial free energy in Eq. (14.27) as a function of temperature. The two components in Eq. (14.27) consist of (a) the first and last terms, which represent the free-energy difference between the homogeneous metastable solution with solute concentration X_i and the equilibrium homogeneous solution of concentration X_α, and (b) the middle term, which is the free-energy change associated with the concentration difference between adjacent parallel planes in the interfacial region. For a solid solution with a positive heat of mixing as required to form a miscibility gap, both terms are always positive. Figure 14.10 shows the contributions of these two terms to the interfacial energy for a (111) interface as a function of temperature, where the first and last terms in Eq. (14.27) are labeled $\Sigma\Delta G_i$ and the middle term is identified as $\Sigma(\Delta X_{i-1})^2$. The free energy increase from segregation to the interface is maximum at $0.5T/T_c$, whereas that associated with the concentration difference decreases steadily with temperature. The two contributions are nearly equal above

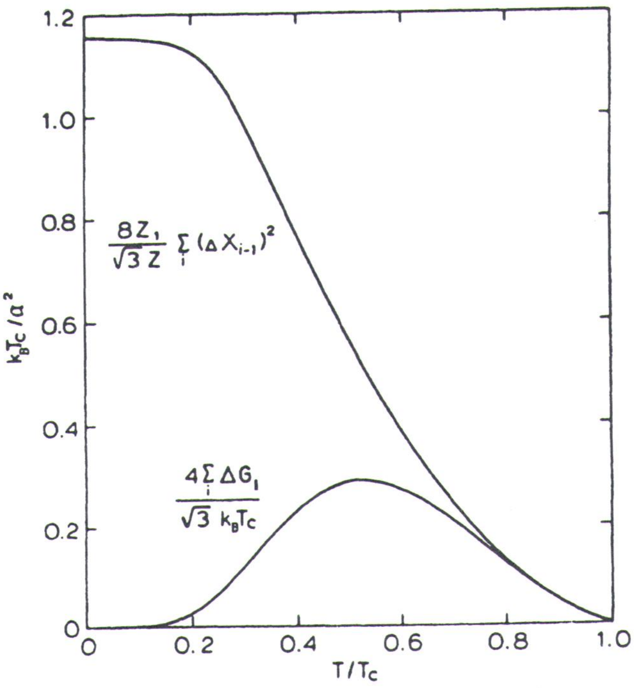

Figure 14.10. Comparison of the two contributions to γ_c^{SS} for the (111) f.c.c. interface. Reprinted with permission from [105] by Elsevier Science Ltd., Oxford, England.

approximately $0.6T/T_c$ and the sum of the two curves in Figure 14.10 gives curve (a) in Figure 14.9.

14.3. ROUGHENING AND PHASE TRANSFORMATIONS AT INTERPHASE BOUNDARIES

Heterophase interfaces roughen and facet just like the solid surfaces (Section 4.2) and homophase interfaces (Section 13.2.6) discussed previously. It is possible to use the Wulff construction discussed for solid surfaces in Section 3.5 to construct the equilibrium shapes of coherent precipitates in solids, such as the G.P. zone in Figure 12.3. Figure 14.11 shows the equilibrium shapes of a coherent f.c.c. precipitate as a function of temperature obtained from the γ plots in Figure 14.8. At 0 K the shape determined from the Wulff construction is seen to be entirely faceted, as shown by the two-dimensional Wulff construction in Figure 14.11a and the faceted particle in Figure 14.11b. The larger facets are {111} and the smaller ones are {100}. At $0.25T_c$ in Figure 4.63c, the Wulff shape becomes a faceted sphere, with the {111} facets still larger than {100}. Increasing the temperature to $0.5T_c$ is seen to com-

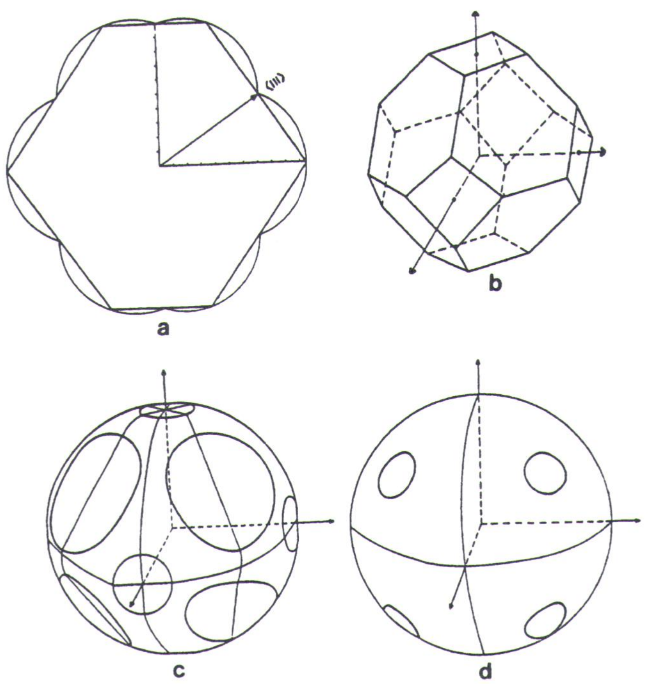

Figure 14.11. (a) (110) section of the polar γ plot for an f.c.c. crystal at 0 K and the corresponding Wulff construction. The corresponding three-dimensional precipitate shapes at 0 K, $0.25T_c$ and $0.5T_c$ are shown in (b), (c) and (d), respectively. From [108].

pletely eliminate the {100} facets and considerably reduce the {111} facets as shown in Figure 14.11d. The shape at $0.75T_c$ (not shown) is essentially spherical.

An example of the roughening of silver-rich G.P. zones as a function of temperature in the aluminum–silver system (Figure 12.3) is shown in Figures 14.12 and 14.13. Figure 14.12 shows <110> bright-field TEM images of two samples aged at 160°C and 350°C to form well-developed G.P. zones. Note that the G.P. zones appear more angular in the sample aged at 160°C. The diffraction pattern shown in the figure exhibits diffuse scattering in the {111} and {100} directions around the fundamental spots because of the {111} and {100} facets. Figure 14.13a shows the measurement technique used to determine the percentage of faceting from the <110> projection of the G.P. zones, and Figure 14.13b shows the experimental results on faceting obtained as a function of aging temperature. These data clearly show the strong temperature dependence of faceting as calculated from the regular-solution DLP model in Figure 14.11. The percentage of {111} facets is greater than {100} and persists to higher temperatures, as predicted from the calculations. Some faceting of the G.P. zones remained up to the solvus, which is just above 350°C. These results were in qualitative agreement with regular solution DLP calculations that were performed using thermodynamic data for the aluminum–silver system [109].

The temperature dependence of faceting shown for the coherent interphase boundary above also occurs for semicoherent and incoherent interfaces, although only a few examples have been documented so far. A second example of solid–solid interfacial roughening with temperature is shown for germanium precipitates in aluminum in Figure 14.14. In contrast to the aluminum–silver G.P. zones above, the germanium precipitates have incoherent interfaces, as shown in Figure 12.6, but form as highly faceted octahedral particles at room temperature. When viewed along a <110> direction in the TEM the octahedra project as squares with edges parallel to {110}, as in Figure 14.14a.

Figures 14.14a–f show the shape evolution of an octahedral particle as a function of temperature studied by *in situ* thermal cycling in a high-voltage TEM. When the germanium particle was heated to a high temperature as in Figure 14.14b, the particle gradually rounded and obtained a nearly spherical shape. Upon subsequent cooling, the precipitate regained its octahedral shape as in Figure 14.14c. This cycle was performed many times (Figs. 14.14d and e). It was also found that if the particle was cycled just a few degrees to either side of the roughening temperature, it changed shape from an octahedron to a sphere without changing its volume. This feature discounted the possibility that the particle was becoming rounded from dissolution and demonstrated that it was displaying a real faceting–roughening transformation. This observation is very similar to the same phenomena previously discussed for solid–vapor (Section 4.2) and solid–liquid (Section 9.4) interfaces. In summary, solid–solid interfaces display faceting and roughening as a function of temperature, and this behavior can be predicted for coherent interfaces using a regular-solution DLP model, which is essentially a bond counting model that accounts for compositionally wrong bonds across the interface.

It is possible to imagine a number of other types of phase transformations that

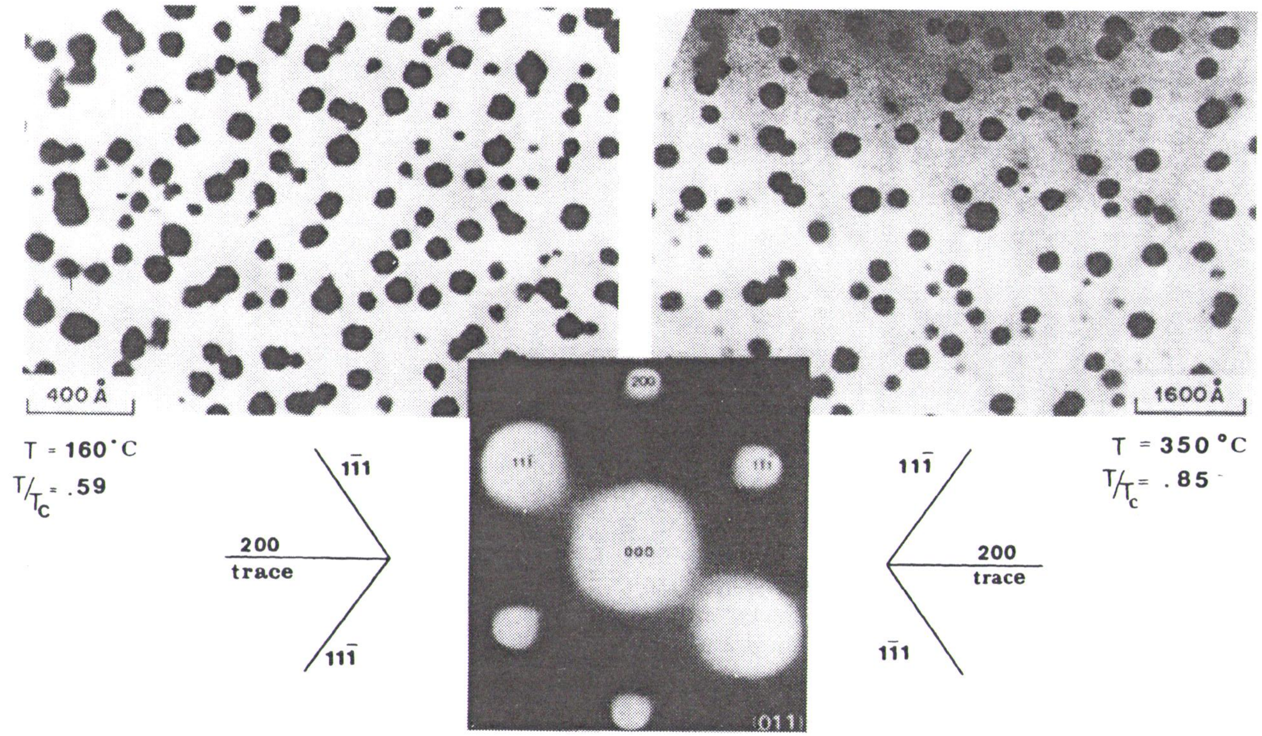

Figure 14.12. Bright-field <110> TEM images of G.P. zones aged at 160°C (0.59T_c) and 350°C (0.85T_c) in aluminum–silver alloy. Reprinted with permission from [109] by Elsevier Science Ltd., Oxford, England.

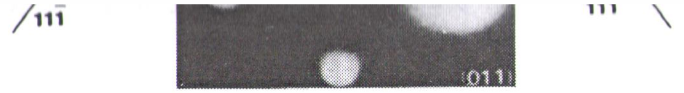

Figure 14.12. Bright-field <110> TEM images of G.P. zones aged at 160°C ($0.59T_c$) and 350°C ($0.85T_c$) in aluminum–silver alloy. Reprinted with permission from [109] by Elsevier Science Ltd., Oxford, England.

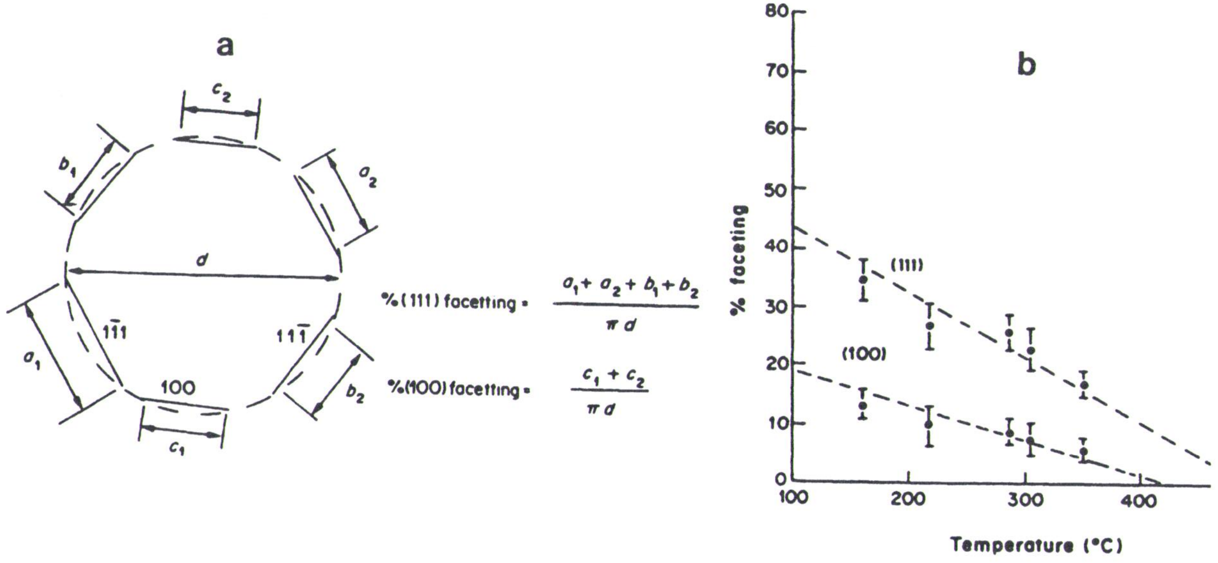

Figure 14.13. (a) Measurement technique for determining the percentage of {111} and {100} facets on the G.P. zones. (b) Percent faceting versus temperature using the measurement technique in (a). The error bars represent the standard devation of the experimental measurements. Reprinted with permission from [109] by Elsevier Science Ltd., Oxford, England.

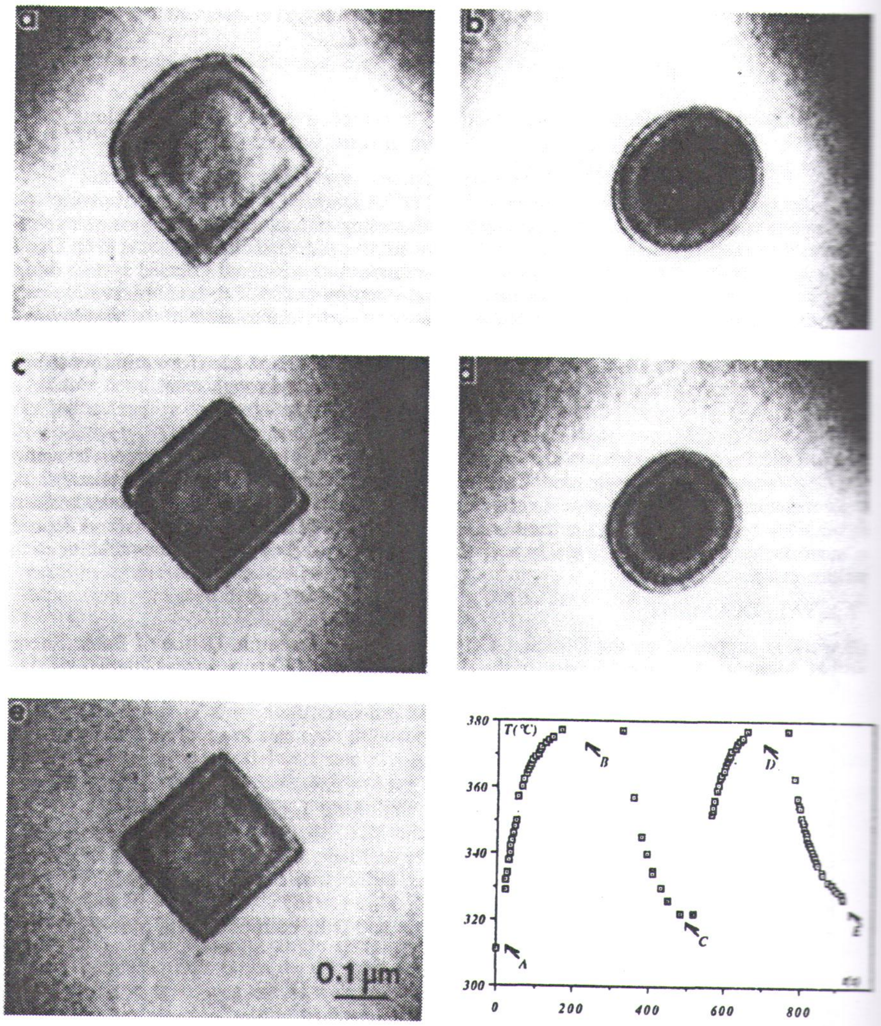

Figure 14.14. (a)–(e) Bright-field TEM images of a germanium particle in aluminum recorded during *in situ* temperature cycling between about 320° and 380°C showing reversible transformation between octahedral and spherical shapes. The temperature cycle is shown in (f). From [110].

could occur at solid–solid interfaces, but only a few examples have been reported experimentally. To illustrate some additional possibilities, Figure 14.15 shows a segment of a copper–silver interphase boundary, like that in Figure 12.5, in which the misfit dislocations have dissociated to form small microtwins in the interface and also stacking faults out of the boundary. The mechanisms and energetics of these interphase boundary transformations are not fully understood but they clearly occur in actual interfaces.

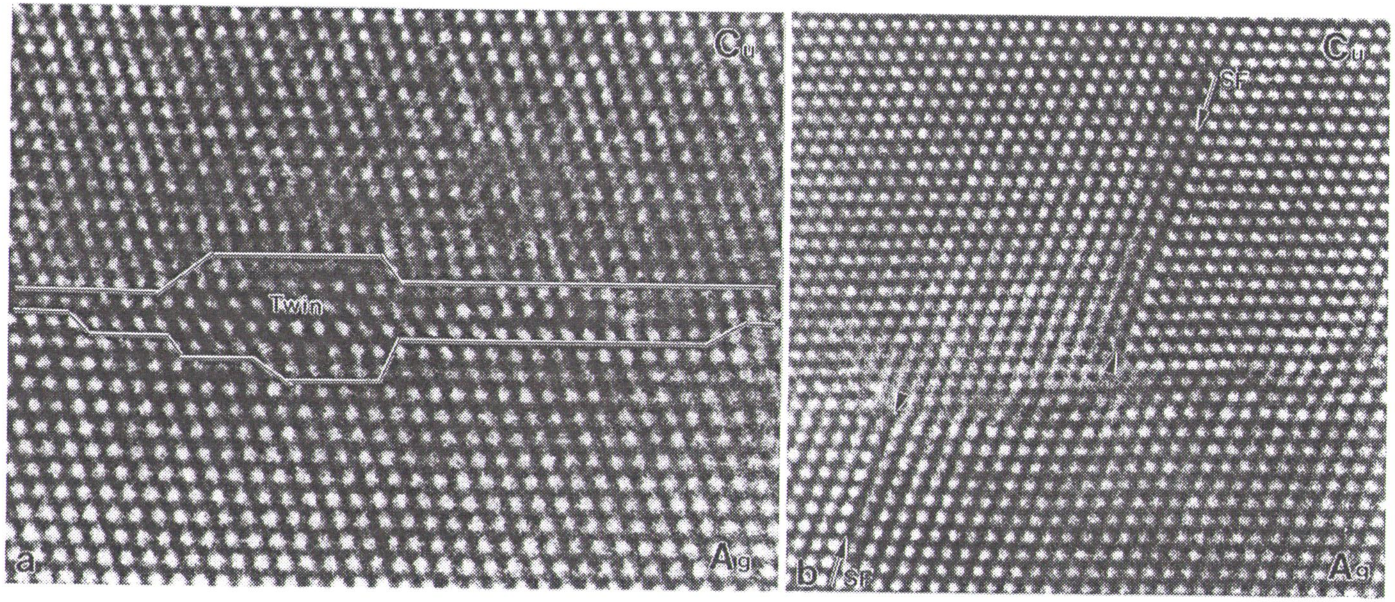

Figure 14.15. HRTEM image of a {111} copper–silver interphase boundary where misfit dislocations have dissociated to form (a) microtwins at the interface (outlined) and (b) stacking faults (arrows). From [111].

14.4. ANTIPHASE BOUNDARIES

An antiphase boundary (APB) separates two domains of the same ordered phase [112,113]. It results from symmetry breaking that occurs during ordering processes, which can start at different locations on a disordered lattice. An APB forms when two such regions contact so that they display wrong compositional bonds across the interface, as illustrated in Figure 14.16. Dislocations with Burgers vectors that are not translation vectors of the ordered superlattice can also create APBs as they move through an ordered phase [112].

Antiphase boundaries are quite similar to the coherent interphase boundaries that were discussed in Section 14.2. We can readily calculate the interfacial energy associated with an APB using a nearest-neighbor broken-bond model. In addition, we can envision the temperature dependence of the APB width by referring to the CH/DLP treatments for coherent interphase boundaries in the previous section and the order parameter introduced in Section 2.6. We examine APBs in an ordered f.c.c. structure in some detail to illustrate these features. This is followed by several examples of the behavior of APBs in f.c.c. alloy systems.

The $L1_2$ structure, or Cu_3Au-type superlattice, is shown in Figure 14.17. The disordered f.c.c. structure transforms to a lower symmetry on ordering, to a simple cubic structure with four atoms or sublattices per primitive lattice point. An A atom occupies one sublattice site in the ordered structure and B atoms occupy the other three sites. Thus, four types of ordered domains can occur on the four sublattices in a crystal: type I with A at 0, 0, 0; type II with A at 0, 1/2, 1/2; type III with A at 1/2, 0, 1/2; and type IV with A at 1/2, 1/2, 0. An APB is produced by an antiphase vector $\mathbf{u}_i$, which brings about the displacement of one atomic species from one sublattice to another. The antiphase vectors correspond to perfect dislocation Burgers vectors in the disordered crystal and are of the type $a/2\langle 110\rangle$ as illustrated in Figure 14.17.

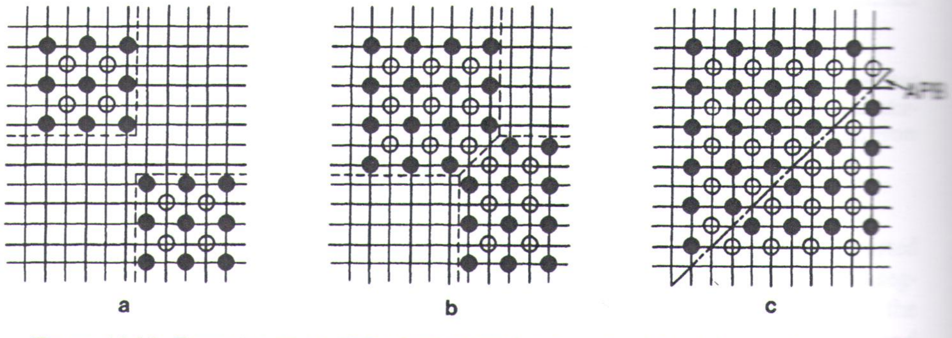

Figure 14.16. Formation of an APB when ordered regions in which A (open circles) and B (filled circles) atoms occupying different sublattices grow together. (a) Nucleation of ordered domains on different sublattices, (b) contact of domains and (c) the resulting APB (dashed line). From [114] reprinted with the permission of Cambridge University Press.

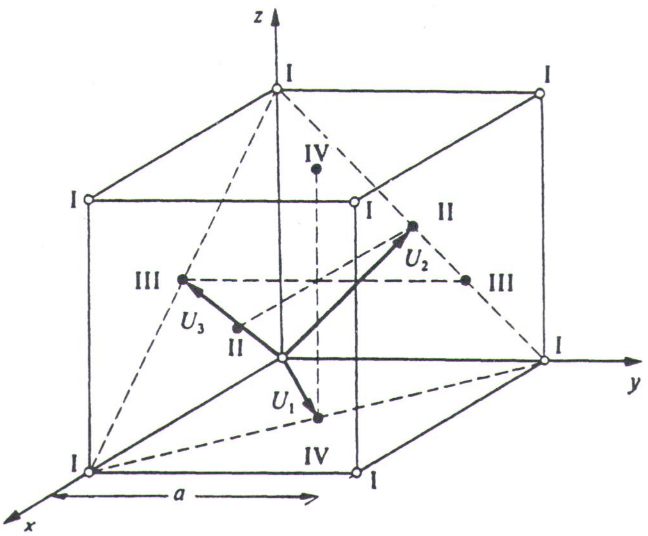

Figure 14.17. Unit cell of the Cu_3Au superlattice. The open and filled circles represent *A* and *B* atoms, respectively. The vectors show equivalent ways of moving an *A* atom from a type I site to type II, III and IV sites. From [114] reprinted with the permission of Cambridge University Press.

An antiphase boundary can be sufficiently described by $\mathbf{u}_i$ and the normal $\mathbf{n}$ to the boundary plane. If $\mathbf{u}_i$ lies in the boundary plane, then

$$\mathbf{u}_i \cdot \mathbf{n} = hu + kv + lw = 0, \tag{14.29a}$$

where $[uvw]$ are the components of the antiphase vector $\mathbf{u}_i$ and (hkl) are the Miller indices denoting the plane of the APB [115]. In this case, the APB is produced by a lattice translation in the boundary plane and there is no net increase or decrease in the number of *A* and *B* atoms at the interface. This type of APB is called a conservative or type 1 APB and a relatively small antiphase boundary energy γ_{apb} is expected for this type of interface. In the second case,

$$\mathbf{u}_i \cdot \mathbf{n} \neq 0 \tag{14.29b}$$

and a nonconservative or type 2 APB boundary results. In this case, it is necessary to remove either a plane of *A* or *B* atoms to form the APB. This leads to an excess or deficit of *A–A* or *B–B* bonds at the interface and a higher energy is expected for this type of APB. Figure 14.17 shows the four sublattices (I–IV) for the $L1_2$ structure with the three associated vectors $\mathbf{u}_i = a/2[110]$, $a/2[101]$ and $a/2[011]$. For an APB with $\mathbf{n} = [001]$, a conservative (type 1) APB is produced by $\mathbf{u}_1$ and the others are nonconservative (type 2).

The antiphase boundary energy γ_{apb} can be estimated as a function of the orientation of the APB (i.e., of the boundary normal **n**, using a nearest-neighbor broken-bond model, similar to the previous cases of solid–vapor and coherent interphase-boundary interfaces). This provides a reasonable estimate of the APB energy at 0 K, because the contribution of higher-order neighbors to the energy is less than 10%. A complete derivation of the equations for APBs in several different f.c.c. and b.c.c. ordered structures is provided by Flinn [115] and Marcinkowski [112]. The derivations are similar to those used in Eqs. (3.20) and (14.22), and we only summarize the end result for the case of the $L1_2$ structure in Figure 14.17 here.

In the case of an $L1_2$ structure with the pair exchange energy ϵ in Eq. (2.19), the APB energy for $\mathbf{u}_1 = a/2[110]$ is given as

$$\gamma_{\mathrm{apb}} = 2\epsilon h \mathfrak{L}^2 / a^2 (h^2 + k^2 + l^2)^{1/2}, \tag{14.30}$$

where $\mathfrak{L}$ is the long-range order parameter (Eqs. 2.29 and 2.30), a is the lattice parameter, and we assume that $h \geq k$. For a conservative $\mathbf{n} = [001]$ APB with $\mathfrak{L} = 1$, $\gamma_{\mathrm{apb}} = 0$, although the APB energy remains finite when next nearest-neighbor interactions are taken into account. The orientation dependence of γ_{apb} for the $L1_2$ structure is shown in Figure 14.18 by lines of constant energy in a stereographic projection of the possible **n**. There is a minimum at $\mathbf{n} = [001]$, maxima at [100] and [010], with saddle points at [110] and $[1\bar{1}0]$.

According to Figure 14.18, APBs in $L1_2$ structures should lie parallel to the cube planes; this has been observed experimentally in alloys where nearest-neighbor bonding interactions are the dominant component to the APB energy. For example, Figure 14.19 shows conventional and high-resolution TEM images of APBs in Cu_3Au. The viewing direction is [001] and the conservative APBs labeled 2 and 3 in Figure 14.19a clearly lie along the cube planes. The white spots in the HRTEM image in Figure 14.19b are the projections of the atomic columns in the structure and the $a/2[110]$ displacement of the white spots across the APBs is directly visible in the image.

More accurate expressions for the antiphase boundary energy that account for the entropy contribution and the presence of extra *A* or *B* atoms at nonconservative APBs have been obtained by Kikuchi and Cahn [113] and Loiseau et al. [116]. At low temperatures, the entropic contribution is small but it can have a substantial effect on the APB profile at temperatures approaching T_c. This effect is illustrated for first-order and second-order ordering reactions in copper–palladium and iron–aluminum alloys, respectively, below [116].

The long-range order parameter $\mathfrak{L}$ as a function of temperature for a second-order order–disorder transformation was illustrated in Figure 2.12, where it was seen that disordering is a cooperative phenomenon that progresses rapidly as T approaches T_c. The degree of order across an APB as a function of temperature can be represented schematically by an order-parameter profile, as shown in Figure 14.20. At 0 K in Figure 14.20a, the order parameter $\mathfrak{L}$ jumps discontinuously from −1 to +1 across the APB, similar to the composition profile across a coherent α–β interphase boundary at 0 K in Figure 14.1. As the temperature is raised, the long-range order parameter decreases, and the APB obtains a finite width L_{apb}. The order-para-

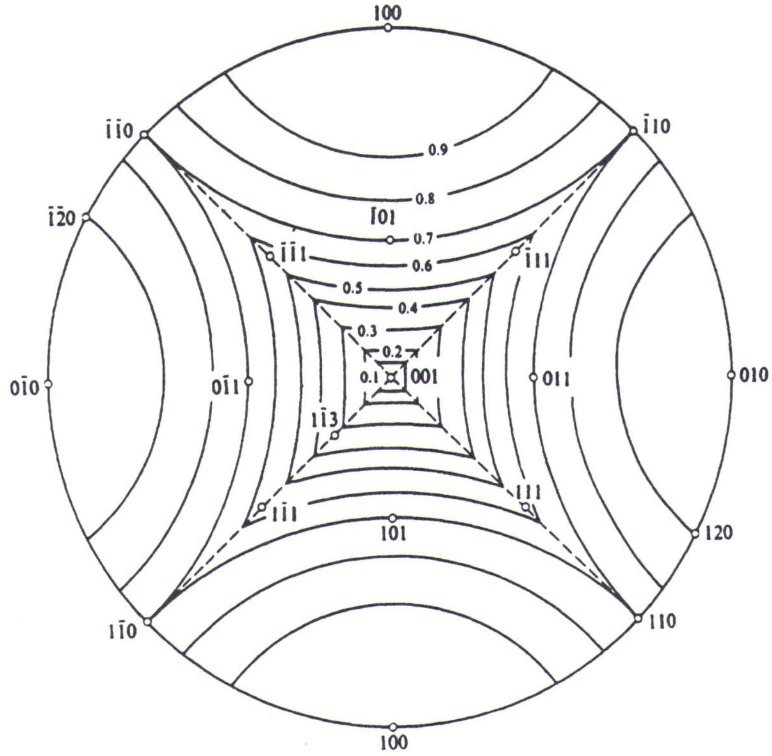

Figure 14.18. Lines of constant APB energy created by $\mathbf{u}_1 = a/2[110]$ in Cu_3Au as a function of the plane normal [*hkl*]. From [114] reprinted with the permission of Cambridge University Press.

meter profile across the APB then looks like T_1 in Figure 14.20b. This profile has the same shape as the composition profile for the coherent α–β interface in Figures 14.3 and 14.7. The long-range order parameter continues to decrease and the APB width continues to increase with temperature, that is, T_2 in Figure 14.20b, until at T_c, $\mathfrak{L} \to 0$, $L_{apb} \to \infty$ and the APB vanishes.

This process is illustrated experimentally for the $DO_3 \to B2$ ordering transformation in an iron–27% aluminum alloy in Figure 14.21. In this system, T_c = 547°C, and the appearance of the APB as a function of temperature was studied *in situ* in the TEM using a heating holder. The APB in the DO_3 structure is dark and the ordered domains ($+\mathfrak{L}$ and $-\mathfrak{L}$) are bright in Figure 14.21a, which is 20°C below T_c. As the temperature is raised in Figures 14.21b–d, the APB width increases and fluctuations in the contrast of the ordered domains also increase. Just below T_c in Figure 14.21d, the image contrast in the domains is beginning to break up and the APB is barely visible. This phenomenon continued until T_c, where the APB vanished. A log–log plot of the APB width as a function of $(T_c - T)$ in this case indicated that L_{apb} obeyed a power law with an exponent between approximately 0.5 and

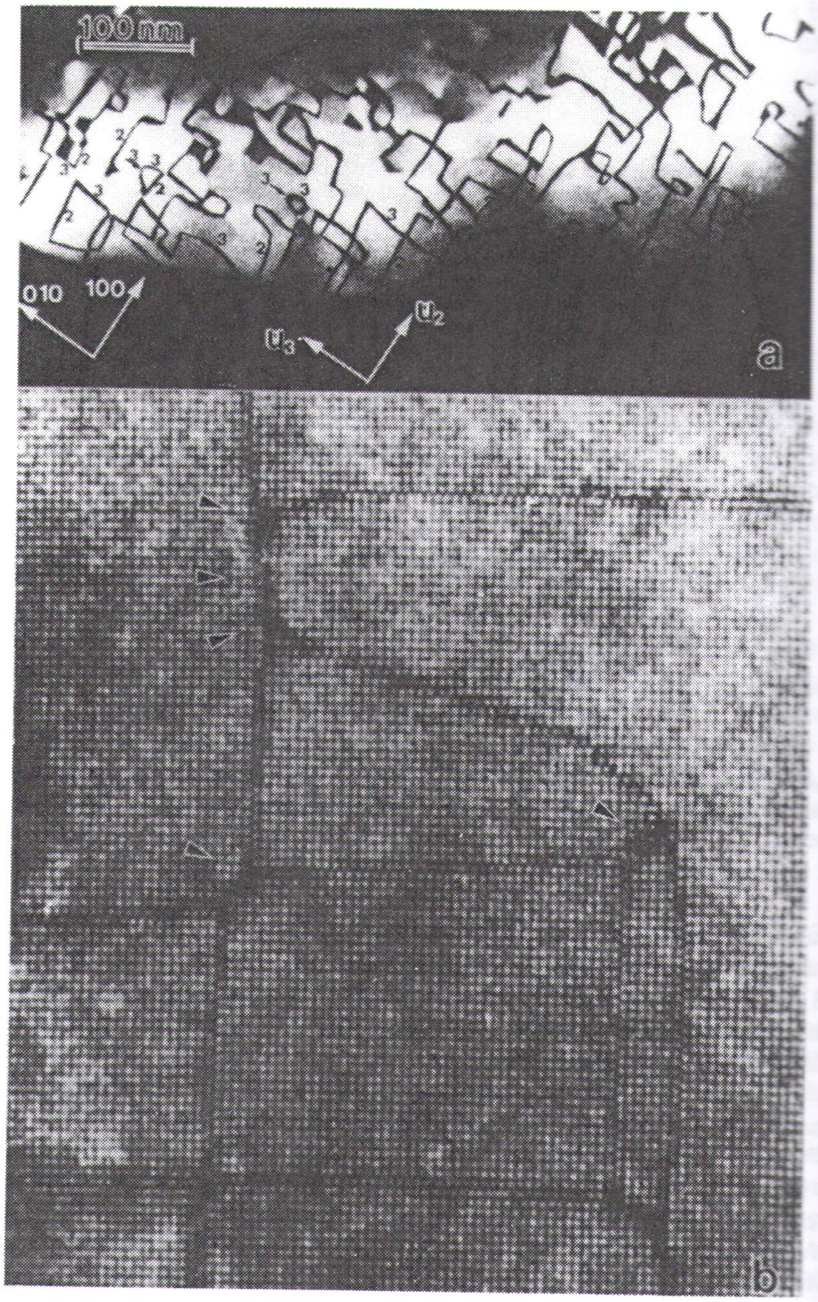

Figure 14.19. (a) (110) dark-field TEM image of APBs in Cu$_3$Au projected along [001]. The numbers 2 and 3 indicate APBs with antiphase vectors $\mathbf{u}_2$ and $\mathbf{u}_3$. Examples of nonconservative APBs are indicated by arrows. (b) [001] HRTEM image showing conservative APBs along (100) and (010) joining at four-point and triple-point junctions (arrows). From [116].

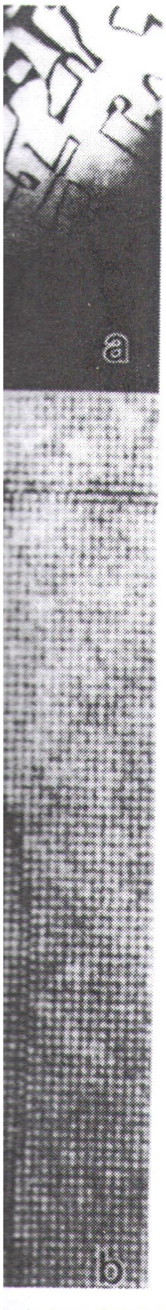

ted along [001]. The
les of nonconserva-
ervative APBs along
m [116].

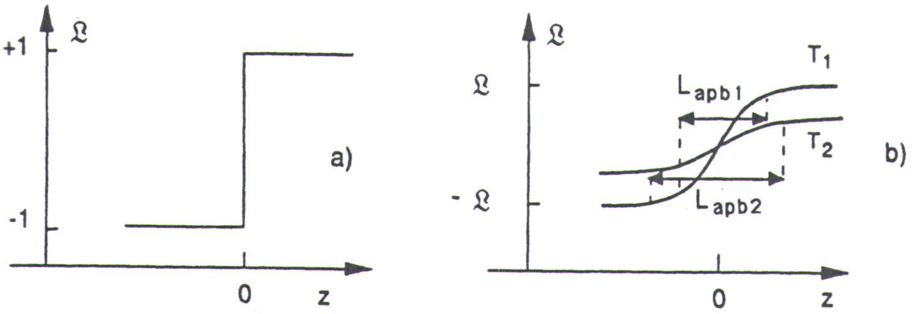

Figure 14.20. (a,b) Evolution of the order-parameter profile of an APB for a second-order transformation with $T_1 < T_2$. From [116].

0.64, similar to the coherent interface in Eq. (14.18) and close to the theoretically predicted value of 0.63 [116,117].

The behavior of an APB in the case of a first-order order–disorder transformation (Fig. 2.13) is more complicated than for a second-order transformation, but it can be qualitatively described for $L1_2$ phase as follows [113,116]. It is possible to sketch an order-parameter profile across an APB as a function of temperature for a first-order reaction, as shown in Figure 14.22. At 0 K in Figure 14.22a, the order parameter changes abruptly from its value in one domain to that in the adjacent do-

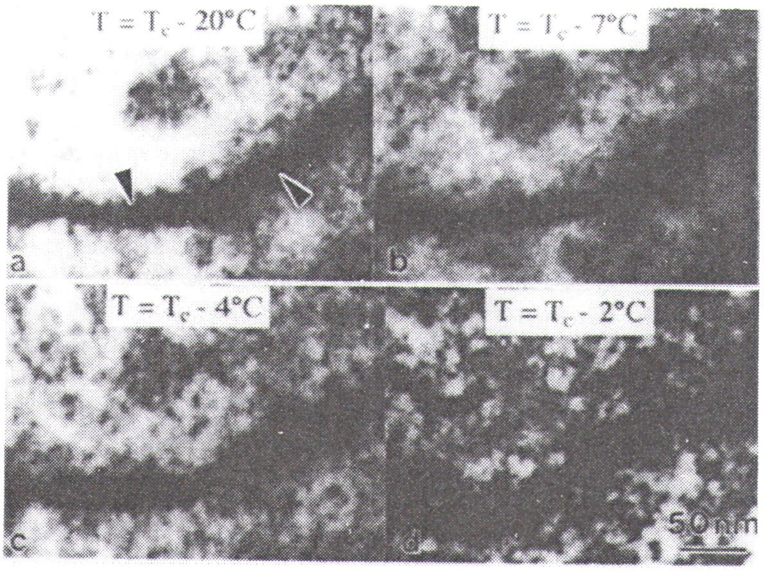

Figure 14.21. (a–d) 1/2(111) dark-field TEM images of an APB in the DO_3 superlattice as a function of temperature approaching T_c. From [116].

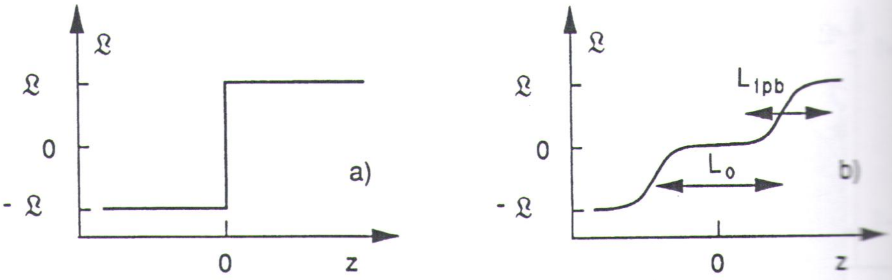

Figure 14.22. (a,b) Evolution of the order-parameter profile of an APB for a first-order transformation. From [116].

main across the APB, similarly to Figure 14.20a. As the temperature is increased to slightly below T_c, the APB progressively splits into two new interphase boundaries (IPB) of thickness L_{ipb} bounding a region of width L_0, where the order parameter is zero, as illustrated in Figure 14.22b. In essence, the APB has become perfectly wet by the disordered f.c.c. phase and the ordered and disordered phases coexist. As T_c is approached, L_{ipb} remains finite but L_0 diverges so that the disordered area becomes large compared to the domain size.

Evidence for this phenomenon has been shown by TEM in several $L1_2$ alloys. An example in a copper–17% palladium alloy is shown in Figure 14.23, where T_c = 506.6°C. In the dark-field TEM images in Figures 14.23a and b, the APBs are visible as gray bands in the image. As the temperature is increased and disorder sets in at the APBs, the APB contrast is replaced by that of a thin, dark disordered film at the boundary (Figs. 14.23c and d); this disorder has been revealed by HRTEM [116]. Between 505.6°C and 506.6°C, the width L_0 rapidly expands, as evident in Figures 14.23e and f, until the entire alloy is disordered at T_c. In contrast to the second-order reaction, the first-order reaction involves nucleation and growth of the disordered phase at the APB and $\mathfrak{L}$ evolves accordingly. The evolution of the APB width L_0 as a function of temperature as $T \rightarrow T_c$ has been determined, and it resembles the graph of the order parameter shown in Figure 2.13.

Thus, we see that the temperature dependence of APBs in a second-order order–disorder reaction is similar to that of coherent interphase and solid–vapor interfaces, whereas the first-order reaction behaves somewhat differently because it involves nucleation and growth. In the second-order reaction, the APB roughens and eventually becomes indistinguishable from the adjacent phases, just like the previous coherent interfaces. In both cases, the APB width increases with temperature.

14.5. SEMICOHERENT INTERPHASE BOUNDARIES

Coherent interphase boundaries form in solids when the lattice parameters of the α and β phases are similar, and there is only a small amount of misfit across the interface. This situation frequently occurs with small or plate-shaped precipitates

---

Figure 14.
tion of the
(d) 505.2°C

and lattic
interphas
other cas
unstraine
of interfa
nite subst
interface
12.5.

Wh
ferred to
herent int
considere

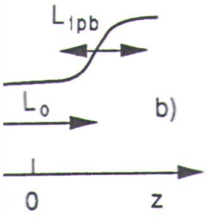

or a first-order trans-

ture is increased to
:rphase boundaries
order parameter is
:ome perfectly wet
ases coexist. As T_c
isordered area be-

several $L1_2$ alloys.
14.23, where T_c =
the APBs are visi-
nd disorder sets in
disordered film at
ealed by HRTEM
ınds, as evident in
contrast to the sec-
and growth of the
lution of the APB
ined, and it resem-

a second-order or-
solid–vapor inter-
ntly because it in-
APB roughens and
just like the previ-
ith temperature.

parameters of the
f misfit across the
haped precipitates

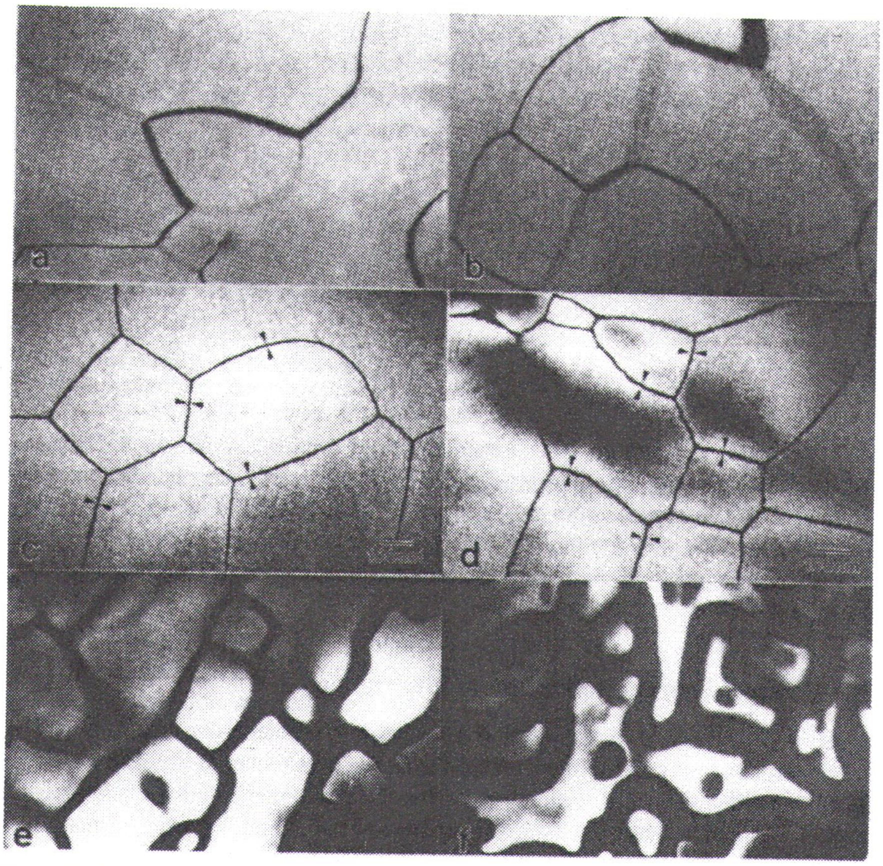

Figure 14.23. (110) dark-field TEM images in copper-17% palladium alloy showing the evolution of the APB contrast as a function of temperature: (a) 498.60°C, (b) 502.6°C, (c) 503.85°C, (d) 505.2°C, (e) 506.1°C and (f) 506.55°C. From [116].

and lattice-matched semiconductors, for example, and two examples of coherent interphase boundaries were shown previously in Figures 12.3 and 12.4. In many other cases, there is sufficient lattice mismatch that coherent interfaces relax to an unstrained condition with an array of misfit dislocations at the interface. This type of interface was illustrated schematically for the case of a thin film on a semiinfinite substrate in Figure 7.7 and an experimental HRTEM image of a semicoherent interface in the copper–silver (f.c.c.–f.c.c.) system was shown previously in Figure 12.5.

When an interface relaxes and acquires a series of misfit dislocations, it is referred to as a semicoherent (discommensurate) interface. The energy of a semicoherent interface between two phases α and β, which differ in composition, can be considered to contain two parts, one associated with the structural defects at the interface and the other due to the unfavorable compositional bonds across the interface. In the previous section on coherent interphase boundaries (Section 14.2), we discussed several procedures that were developed to calculate the interfacial energy from compositional differences across an interface. In this section, we examine a treatment that was developed to quantify the elastic strain energy associated with a semicoherent interface.

Turnbull [118] suggested that when the misfit is small, it is reasonable to assume that the interfacial energy of a semicoherent interface γ_{sc}^{SS} can be determined by adding the compositional γ_{c}^{SS} and structural γ_{s}^{SS} (elastic strain) components together to obtain the total interfacial energy. In equation form this can be expressed as

$$\gamma_{sc}^{SS} = \gamma_{c}^{SS} + \gamma_{s}^{SS}. \tag{14.31}$$

We begin this section by determining the structural component of the interphase boundary energy. We then combine this with the compositional component to obtain the total interphase boundary energy of a semicoherent interface according to Eq. (14.31). We also compare the relative magnitudes of the compositional and structural components to the interphase boundary energy in an f.c.c.–f.c.c. system as a function of misfit and temperature.

14.5.1. Geometry of Semicoherent Interfaces

In Eq. (4.21), we defined the misfit δ between a substrate and a thin film as $\delta = (\alpha_f - \alpha_s)/\alpha_s$, where α_f and α_s represented the lattice parameters of the film and substrate, respectively. In this section, we define the same misfit, but we use the subscripts 1 and 2 to indicate the lattice parameters of the α and β phases, respectively, which are both assumed to be semiinfinite in extent except when noted otherwise. For simplicity, we will let the α and β phases be simple cubic crystals aligned across the interface and differing only in lattice parameter, as illustrated in Figure 14.24. We then follow the approach of Frank and van der Merwe [119,120] in analyzing the resulting interfacial structure and energy, as summarized in a review by Aaronson et al. [121].

We are interested in the situation where there is relatively strong bonding across the α–β interface so that relaxation of the interface occurs and the misfit is localized at dislocations in the interface, as illustrated in Figure 14.24. In between the dislocations, the planes in the two lattices match perfectly. Designating the lattice parameter of the α phase as α_1 and that of the β phase as α_2, the repeat distance D_δ between the dislocations (or alternatively, between the regions of perfect matching) is given by

$$D_\delta = n\alpha_1 = (n+1)\alpha_2, \tag{14.32}$$

where n represents an integral number of spacings in either lattice. Because the interfacial dislocations are derived from the difference in lattice parameters across the

nds across the inter-
s (Section 14.2), we
he interfacial energy
ction, we examine a
gy associated with a

t is reasonable to as-
$^{IS}_{c}$ can be determined
ain) components to-
his can be expressed

(14.31)

nponent of the inter-
itional component to
t interface according
e compositional and
n f.c.c.–f.c.c. system

d a thin film as δ =
of the film and sub-
, but we use the sub-
phases, respectively,
hen noted otherwise.
ıbic crystals aligned
illustrated in Figure
we [119,120] in ana-
arized in a review by

ively strong bonding
curs and the misfit is
re 14.24. In between
. Designating the lat-
$_2$, the repeat distance
ons of perfect match-

(14.32)

ttice. Because the in-
parameters across the

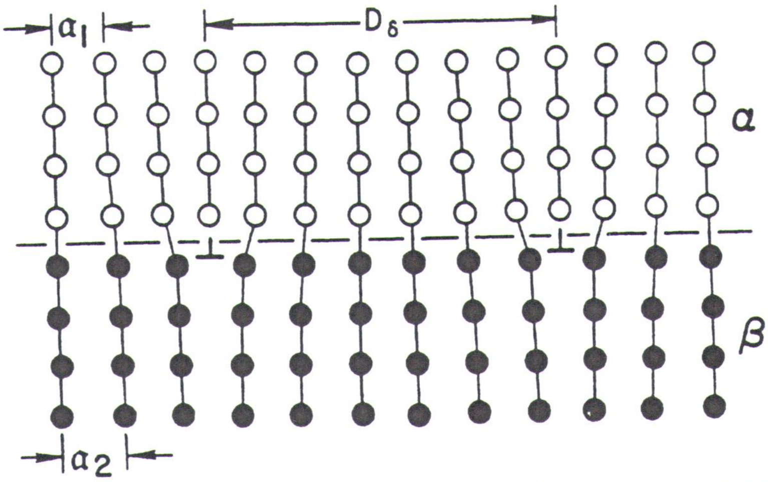

Figure 14.24. Atomic model of a semicoherent interface in a simple cubic crystal where $\alpha_\beta > \alpha_\alpha$. Reprinted from [127] with kind permission from Elsevier Science S.A., Lausanne, Switzerland.

interface they are commonly called misfit dislocations. Unlike isolated dislocations which increase the energy of a single-phase material, these dislocations are an energy-reducing feature of the structure.

It is sometimes convenient to quantify the misfit between two lattices in terms of a reference lattice that is an average of the two lattices rather than in terms of one or the other of the two lattices as in Eqs. (4.21) or (14.32). If we use an average reference lattice, its lattice parameter is given by

$$\alpha' = \frac{\alpha_1 + \alpha_2}{2} \tag{14.33}$$

and with this, Eq. (14.32) becomes

$$D_\delta = (n + 1/2)\alpha'. \tag{14.34}$$

Noting that

$$n = \frac{\alpha_2}{(\alpha_1 - \alpha_2)} \tag{14.35}$$

and substituting into Eq. (14.33) leads to the following expression for the repeat distance,

$$D_\delta = \frac{(\alpha_1 + \alpha_2)^2}{4(\alpha_1 - \alpha_2)}. \tag{14.36}$$

The misfit δ between the α and β lattices can then be defined by the ratio of the reference lattice parameter to the repeat distance, or $\delta = \alpha'/D_\delta$. Thus,

$$\delta = \frac{2(\alpha_1 - \alpha_2)}{\alpha_1 + \alpha_2} = \frac{\alpha_1 - \alpha_2}{\alpha'} \tag{14.37}$$

and the misfit is given as the ratio of the difference in the α and β lattice parameters to the parameter of the reference lattice. Note that the lattice parameters are given in units of length (nanometers) so that δ is dimensionless. Rewriting Eq. (14.36) on the basis of Eq. (14.37) gives the misfit dislocation spacing at the interphase boundary as

$$D_\delta = \alpha'/\delta = b/\delta, \tag{14.38}$$

where b is the magnitude of the edge component of the Burgers vector **b** of the misfit dislocation. Physically, this equation is analogous to Eq. (13.2b) developed for a grain boundary, with the rotation θ replaced by the misfit δ.

14.5.2. Energy of Semicoherent Interfaces

The energy of a semicoherent interface was first analyzed by Frank and van der Merwe [119,120]. Their treatment yields an equation that is physically analogous to Eq. (7.8), but it is more sophisticated and contains higher-order terms. In the treatment of Frank and van der Merwe, misfit is considered in only one direction as in Figure 14.24 and atomic relaxation is permitted in the vicinity of the misfit dislocations. The interaction of the atoms across the interphase boundary is assumed to occur according to a sinusoidal force law and the interaction within a given phase is treated on the basis of an elastic continuum. Their approach yields the following expression [122] for γ_s^{SS}, the misfit dislocation energy at the α–β boundary:

$$\begin{aligned}\gamma_s^{SS} = \mu\alpha'/4\pi^2\{1 + \Lambda - (1 + \Lambda^2)^{1/2} \\ - \Lambda \ln[2\Lambda(1 + \Lambda^2)^{1/2} - 2\Lambda^2]\},\end{aligned} \tag{14.39a}$$

where

$$\Lambda = 2\pi\delta(C_\delta/\mu) \tag{14.39b}$$

$$1/C_\delta = [(1 - \nu_\alpha)/\mu_\alpha] + [(1 - \nu_\beta)/\mu_\beta] \tag{14.39c}$$

and μ is the shear modulus at the interface, μ_α and μ_β are the shear moduli and ν_α and ν_β are Poisson's ratios in the α and β phases, respectively. The C_δ term accounts for elastic interactions within each crystal whereas μ accounts for such interactions across the α–β interface. When these individual characteristics are suppressed by letting $\nu_\alpha = \nu_\beta = 1/3$ and $\mu_\alpha = \mu_\beta = \mu$, then $\Lambda = 3\pi\delta/2$ and γ_s^{SS} is only a function of

y the ratio of the ref-
us,

(14.37)

l β lattice parameters
rameters are given in
iting Eq. (14.36) on
he interphase bound-

(14.38)

; vector **b** of the mis-
.2b) developed for a

Frank and van der
sically analogous to
r terms. In the treat-
y one direction as in
of the misfit disloca-
ry is assumed to oc-
hin a given phase is
lds the following ex-
boundary:

(14.39a)

(14.39b)

(14.39c)

shear moduli and ν_α
he C_8 term accounts
for such interactions
s are suppressed by
is only a function of

μ and δ. The solid curve in Figure 14.25a shows the variation of γ_s^{SS} with δ under these conditions. It is particularly important to note the rapid increase in γ_s^{SS} with δ when $\delta < 0.01$ and the small dependence of γ_s^{SS} on δ at larger misfits. Also note the energy reaches a maximum of $\mu a'/4\pi^2$, or the first term in Eq. (14.39a). Van der Merwe [122] has shown that at least 98% of the total elastic strain energy is stored within the region $x \leq D_\delta/2$, where x is the distance normal to the interface.

It is common to find misfit in two mutually perpendicular directions as in the {100} interphase boundary in semiconductor crystals, and also in three directions 120 degrees apart as between the close-packed {111} and (0001) planes of cubic and hexagonal crystals, for example. Thus it is possible to have interfacial dislocation networks such as those illustrated in Figure 14.26. When there are two perpendicular sets of parallel edge dislocations (Fig. 14.26b) each having an energy expressed by Eq. (14.39), to first approximation the interaction energy between the two sets of dislocations can be neglected and the energy of the two sets of dislocations can be added to give the structural part of the interfacial energy as $2\gamma_s^{SS}$. The example of three sets of dislocations in Figure 14.26c is more complicated since the Burgers vectors have mutual components and the interaction energy is not negligible.

It is also important to consider the effects of the other factors such as the elastic moduli on the interfacial energy γ_s^{SS}. The ratio μ_α/μ_β is referred to as the rela-

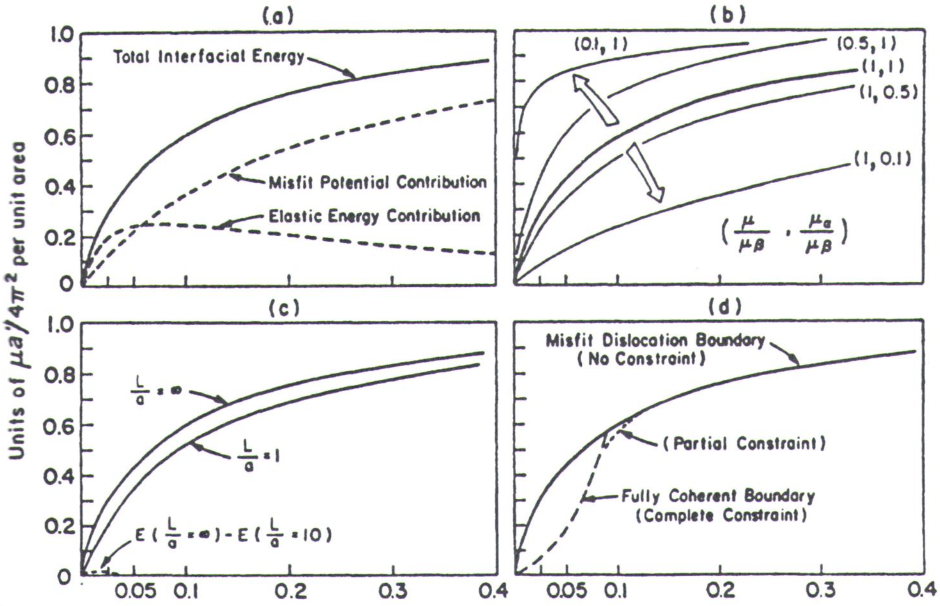

Figure 14.25. Misfit dependence of the dislocation interphase boundary energy γ_s^{SS} as influenced by (a) contributions of the misfit potential and elastic energy, (b) the relative hardness (μ_α/μ_β) and interfacial bonding strength (μ/μ_β), (c) the relative thickness of one component, and (d) the relative elastic strain accommodation. From [121,122].

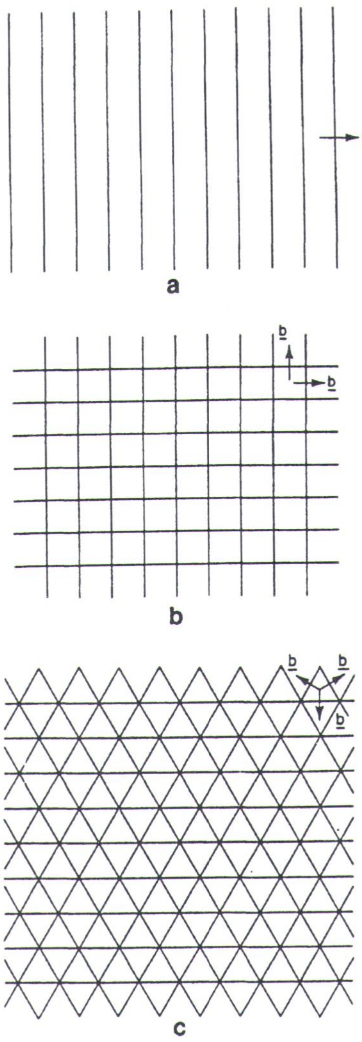

Figure 14.26. Misfit dislocation network for (a) one set of dislocations as in Figure 14.24, (b) two sets of perpendicular dislocations, and (c) three sets of dislocations at 120°. Reprinted from [123] with kind permission from Elsevier Science-NL, Amsterdam, The Netherlands.

tive hardness (or strength) of the two crystals and the ratio μ/μ_β is taken to represent the strength of the interfacial bond. Figure 14.25b shows that, for a constant value of the strengths of the phases (μ_α/μ_β), increasing the strength of the interfacial bond (μ/μ_β) by a factor of ten sharply decreases the initial slope of the γ_s^{SS} versus δ curve and greatly extends the range over which γ_s^{SS} increases appreciably with δ. In comparison, for a constant value of μ/μ_β, increasing μ_α/μ_β produces an increase in the curve and a decrease in the range where γ_s^{SS} depends on δ.

as in Figure 14.24, (b)
ns at 120°. Reprinted
The Netherlands.

μ_β is taken to repre-
that, for a constant
ength of the interfa-
lope of the γ_s^{SS} ver-
ses appreciably with
$/\mu_\beta$ produces an in-
ds on δ.

Another situation that is important to consider, is when the thickness L of one of the phases, say the α phase, is less than the interdislocation spacing D_δ. This situation is encountered in thin films, as discussed in Section 7.2, and also applies to small misfitting precipitates in a matrix. Figure 14.25c shows that when the α and β phases differ only in lattice parameter, γ_s^{SS} is less in a monatomic film that in one of semiinfinite thickness only at small values of δ. When $L/\alpha \cong 20$ the difference becomes negligible throughout the range of misfit.

When both L and δ are sufficiently small, a fully coherent interface has a lower energy than one with an equilibrium arrangement of misfit dislocations. A qualitative argument upon which this conclusion is based is illustrated in Figure 14.25d. The energy of a fully coherent interface increases proportionally to δ^2 (Eq. 7.8) and, therefore, increases slowly at small misfits, whereas that of a misfit dislocation boundary exhibits a rapid initial rise (Fig. 14.25a). Hence, a misfit dislocation interface does not have a lower energy until a critical value of the misfit is exceeded. Quantitatively, the energy required to deform a thin film homogeneously in one direction is derived from Eq. (7.8) as

$$E_{el} = \frac{\mu_\alpha(1-\nu_\alpha)L\delta'^2}{(1-2\nu_\alpha)}, \tag{14.40}$$

where $\delta' = (\alpha_1 - \alpha_2)/\alpha_1 \cong \delta$ for small values of misfit, α_1 is the lattice parameter of the thin film and α_2 is the lattice parameter of the substrate. The critical value of the misfit δ_c' occurs when E_{el} in Eq. (14.40) is equal to γ_s^{SS} in Eq. (14.39a). Letting $\nu_\alpha = \nu_\beta = \nu$ and considering the misfit to be sufficiently small that $\Lambda^2 \cong 0$ yields the relationship

$$\frac{\ln(4\pi\delta_c'\mu_\alpha)}{(1-\nu)(1+\mu_\beta/\mu_\alpha)\mu} + \frac{2\pi(1-\nu)^2(1+\mu_\beta/\mu_\alpha)L\delta_c'}{(1-2\nu)\alpha_1} = 0. \tag{14.41}$$

If $\nu = 1/3$ and $\mu_\alpha = \mu_\beta = \mu$, the thickness of α phase corresponding to δ_c' is

$$L_c = \frac{3\alpha_1[1 - \ln(3\pi\delta_c')]}{16\pi\,\delta_c'}. \tag{14.42}$$

Figure 14.27 shows the dependence of δ_c' on the ratio L/α_1 when $\mu_\alpha = \mu_\beta = \mu$ and $\nu = 0.3$. This plot shows that it is possible to maintain full coherency of interfaces for significant thicknesses only for small values of the misfit (i.e., when δ_c' is on the order of 1% or less). Since the generation of misfit dislocations requires an activation energy, the fully coherent state is bound to be retained in metastable equilibrium until $(\pi/2)\delta_c'$. Note that the value of L_c depends on the ratios of the elastic moduli in Eq. (14.41). Thus, for a given value of L/α_1, the value of the critical misfit δ_c' increases with the bonding strength (μ/μ_β) for a given level of relative hardness (μ_α/μ_β) and with decreasing relative hardness for a given level of bond strength, both in accord with qualitative expectation.

Examples abound of misfit dislocations at heterophase interfaces, and they

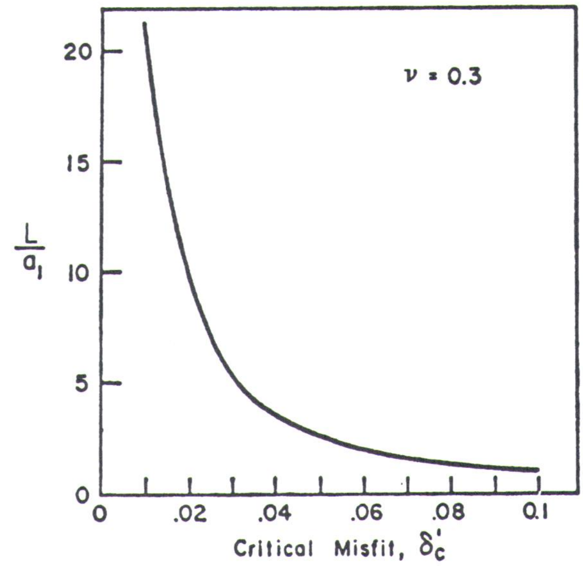

Figure 14.27. Dependence of the critical misfit δ_c' on the ratio of the thickness of one phase L to the interatomic spacing of the phase α_1. From [121,122].

have been compiled in several reviews [121,124,125]. Here we show just one example of a typical interphase boundary dislocation structure to illustrate its appearance in the TEM. Figure 14.28 shows the interfacial dislocation structure formed at the interface between a chromium rod (dark) and the NiAl matrix (light) in a directionally solidified Cr–NiAl eutectic alloy. Both phases in this system are cubic, and they are in a parallel orientation relationship. The misfit is small and the spacing of the interfacial dislocations with **b** = α<100> was found to be quite regular ($D_\delta \sim 120$ nm), as evident in the figure. It is often found that experimentally measured dislocation spacings are greater than those expected from equilibrium elasticity calculations, and this has been attributed to the difficulty of nucleating misfit dislocations at interfaces [121,122].

It is worth noting the similarity of Eq. (14.39a) with the Read–Shockley formula for grain boundaries in Eq. (13.3). For well-separated dislocations and phases with similar elastic moduli where $\mu_\alpha = \mu_\beta = \mu$, Λ reduces to $\Lambda = \pi\alpha'/D_\delta(1 - \nu)$. Furthermore, for $D_\delta >> \alpha'$, higher powers of Λ may be neglected, and, if the misfit δ is substituted for α'/D_δ, then Eq. (14.39a) simplifies [127] to

$$\gamma_s^{SS} = \frac{\mu\alpha'\delta}{4\pi(1-\nu)}(A_0 - \ln\delta), \qquad (14.43)$$

where A_0 is a dislocation core energy. If δ is replaced by θ, the factor $(1 - \nu)$ is replaced by unity, and α' is replaced by b for a homophase system, Eq. (14.43) becomes the formula for a low-angle twist boundary with a rotation angle θ (Eq.

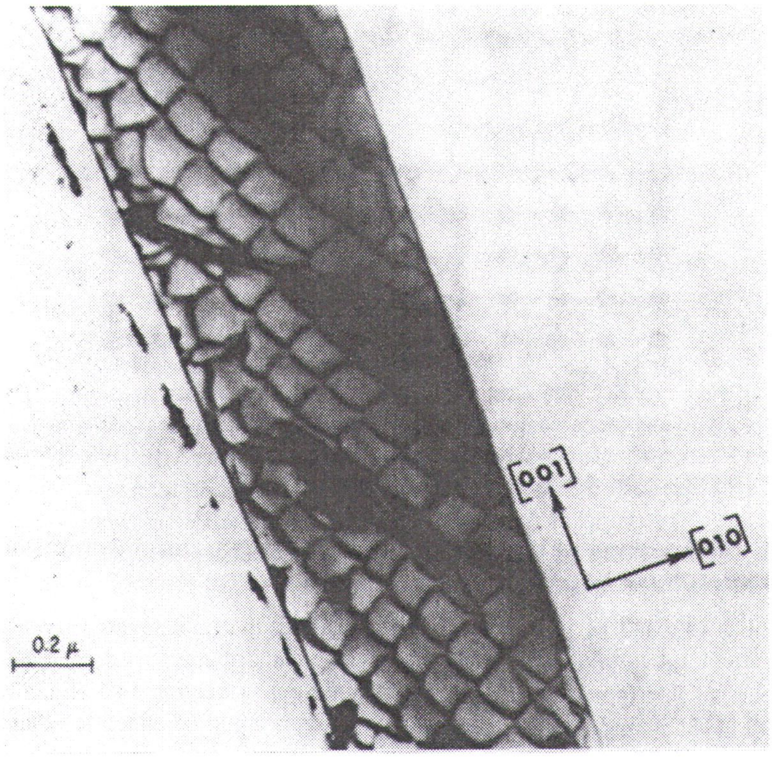

Figure 14.28. Bright-field TEM image illustrating a dislocation network in a directionally solidified Cr-NiAl eutectic quenched from 1200°C. The network is rotated 45° with respect to the rod axis. Reprinted with permission from [126] by Elsevier Science Ltd., Oxford, England.

13.3). Hence, the origin of the interfacial dislocation energies is similar in both homophase and heterophase interfaces.

14.5.3. Incoherent Interfaces

Figure 14.29 shows an incoherent (incommensurate) interphase boundary with an interphase boundary energy γ_i^{SS}. It is different from the semicoherent interface in Figure 14.24 in that the bonding across the interface is sufficiently poor that there is no local relaxation of the misfit into dislocations at the interface. Instead, the misfit is spread evenly across the entire interface and the two phases retain their bulk structures up to the interfacial plane, where they terminate abruptly. This is similar to the krypton–graphite interface shown previously in Figure 4.16b and this type of interface is expected to have a high interfacial energy and low strength. An upper limit on (and fairly reasonable estimate of) γ_i^{SS} can be obtained by adding the surface energies of the two crystallographic faces (*hkl*) of the α and β phases.

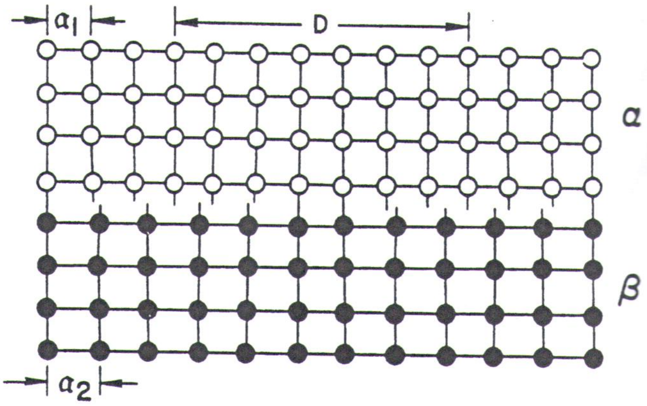

Figure 14.29. Atomic model of an incoherent interface in a simple cubic crystal where $a_\beta > a_\alpha$, and there is very weak interaction across the interface. Reprinted from [127] with kind permission from Elsevier Science S.A., Lausanne, Switzerland.

14.5.4. Comparison of the Compositional and Structural Components of the Interphase Boundary Energy

In Sections 14.2 and 14.5.2, we developed procedures to calculate the compositional and structural components of the interphase boundary energy for coherent and semicoherent interfaces, respectively. As pointed out in Section 14.5 (Eq. 14.31), Turnbull [118] suggested that these two components could be added to obtain the total interphase boundary energy of a semicoherent interface. This procedure has been applied to a few interfaces [128–130]. In this section, we show the results from the most complete analysis of this type, which was performed for a semicoherent f.c.c.–f.c.c. interface using lattice parameters and elastic constants appropriate for copper as a function of temperature and assuming a symmetric regular solution with a critical temperature of 1200 K (corresponding to a regular solution constant of 19.9 kJ/mole). The calculation is described in detail by Spanos [130].

The basic procedure employed in the study was the following. (a) The O-lattice method (Section 13.2.2) was used to determine the dislocation structure of the interphase boundaries between two f.c.c. crystals of identical orientation but with different lattice parameters as a function of boundary orientation. (b) The structural energy of these interfaces was determined by employing elastic energy calculations for dislocation arrays due to Hirth and Lothe (HL) [39] and also according to the van der Merwe analysis (Eq. 14.39) for the {100} interface. (c) The compositional component to the interphase boundary energy was calculated using the regular-solution discrete lattice plane (DLP) model described in Section 14.2.3 (Eq. 14.27) and this was compared with the structural energy obtained for the same boundary as a function of temperature. (d) Polar γ plots were developed for each of these energies in order to compare their anisotropies as a function of temperature. (e) A Wulff construction (Section 3.5) was performed on each polar γ plot for the purpose of comparing the equilibrium shapes yielded by the structural and compositional energies as a function of temperature. (f) The polar γ plots and the Wulff constructions were evaluated for the sum of the structural and compositional interfacial energies.

Table 14.2 compares the magnitudes of the compositional interfacial energy γ_c^{SS} with the structural energy γ_s^{SS} for the DLP and HL methods of calculation for the $\{100\}_{\text{f.c.c.}} \| \{100\}_{\text{f.c.c.}}$ and $\{111\}_{\text{f.c.c.}} \| \{111\}_{\text{f.c.c.}}$ interfaces as a function of reduced temperature T/T_c. These data show that at relatively low misfits (0.2%) the compositional contribution to the interfacial energy dominates, but that for higher values of misfit (2.0%), the structural contribution γ_s^{SS} can be more than twice γ_c^{SS}. With an increase in temperature, there is a large decrease in the compositional part of the interfacial energy, as in Figure 14.9, whereas the structural energy drops off much more slowly. Thus, at higher temperatures, the compositional component should provide a much smaller contribution to the total interfacial energy of a semicoherent interface γ_{sc}^{SS} than the structural component. The structural energy is lowest for the $\{100\}$ interface, and the $\{111\}$ interface has the lowest compositional interfacial energy.

The temperature dependence of the anisotropy of the compositional component of the energy for these interfaces was also found to be much greater than for the structural part. This is illustrated by the $\{011\}$ polar γ plots for the compositional and structural parts of the interfacial energy shown in Figure 14.30. These plots were constructed from 180 different values for γ_s^{SS}. The absence of facets on the two-dimensional Wulff construction of the compositional polar γ plot at $T/T_c = 0.9$ follows directly from the rapid decrease in the anisotropy of γ_c^{SS} as T_c is approached [108]. In contrast, at the same temperature, facets are still present on the two-dimensional Wulff construction for γ_s^{SS}. Also, the bumpiness of the γ_s^{SS} plot is due to the fact that rather small changes in orientation can result in quite different dislocation configurations at the interface [130]. In these studies, the HL analysis for γ_s^{SS} was found to be more reliable at high values of misfit because it accounted for interaction of the misfit dislocations more rigorously than in the van der Merwe analysis.

Results from analysis of the $\{100\}_{\text{f.c.c.}} \| \{100\}_{\text{f.c.c.}}$ interface are shown graphically in Figure 14.31 to illustrate the relative magnitudes of γ_c^{SS}, γ_s^{SS} and γ_{sc}^{SS} (Eq. 14.31) as a function of T/T_c for two levels of room temperature misfit δ^{RT}. The

Table 14.2. Comparison of the DLP model compositional energy [105] and HL [39] structural energy for $\{100\}_{\text{f.c.c.}} \| \{100\}_{\text{f.c.c.}}$ and $\{111\}_{\text{f.c.c.}} \| \{111\}_{\text{f.c.c.}}$ interfaces as a function of reduced temperature T/T_c; RT = room temperature

	γ_c^{SS}		γ_s^{SS} ($\delta^{RT} = 0.2\%$)		γ_s^{SS} ($\delta^{RT} = 2.0\%$)	
T/T_c	$\{100\}$	$\{111\}$	$\{100\}$	$\{111\}$	$\{100\}$	$\{111\}$
0.25	161.9	144.9	45.5	47.3	298.2	318.1
0.50	111.3	107.5	40.1	41.7	265.9	283.2
0.75	45.2	45.3	29.7	30.8	207.2	219.7
0.90	12.4	12.4	21.1	21.9	147.6	155.6

Source: From [130].

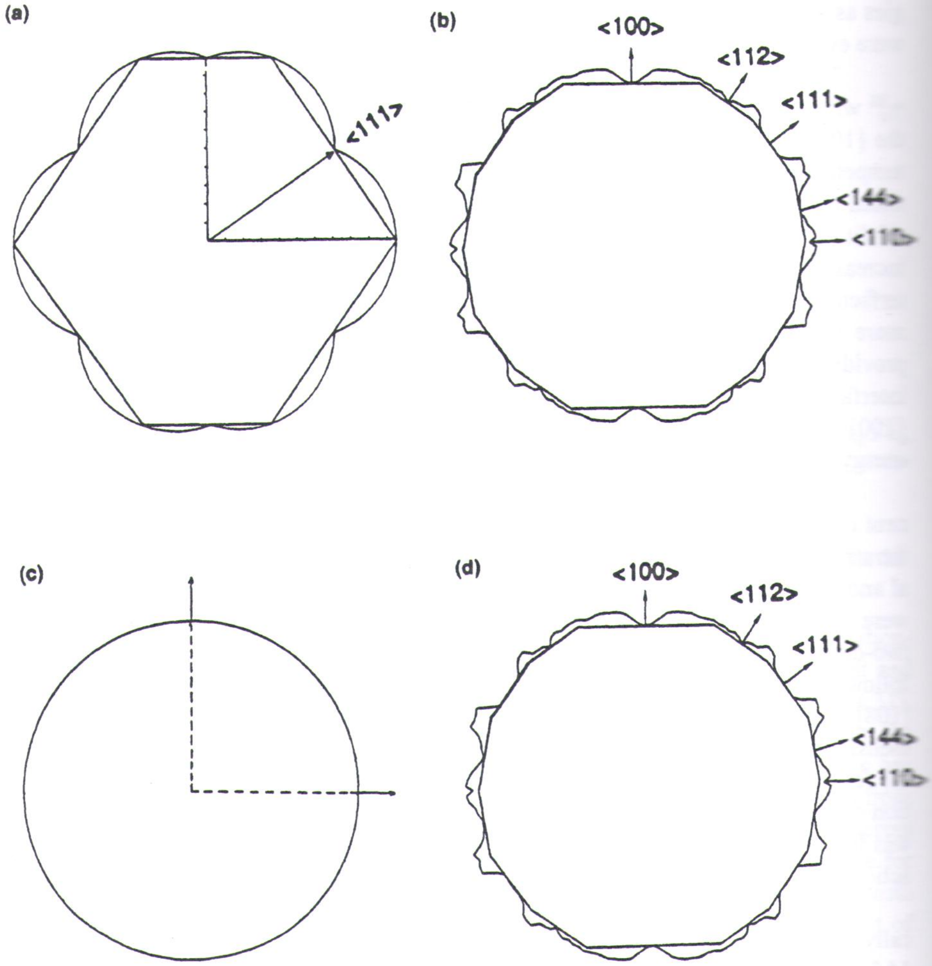

Figure 14.30. Comparison of {011} sections through polar γ plots for γ_c^{SS} and γ_s^{SS} estimated from the DLP model and HL analysis at (a,b) $T/T_c = 0$ and (c,d) $T/T_c = 0.9$. The plots were normalized by the minimum value of the plot. From [130].

structural component is greater than the compositional component at all levels of T/T_c for $\delta^{RT} \geq 1\%$. On the other hand, at $\delta^{RT} = 0.2\%$, $\gamma_c^{SS} > \gamma_s^{SS}$ for all values of T/T_c less than about 0.82. It is important to note that γ_c^{SS} depends on the temperature and shape of the miscibility gap in the regular solution model, which can change appreciably from one system to another, thus influencing the ratio $\gamma_c^{SS}/\gamma_s^{SS}$. These results suggest that γ_c^{SS} is most likely to influence the facets that form at interfaces at temperatures below $0.25T_c$, whereas at temperatures greater than $0.75T_c$ where there is no compositional anisotropy, the structural part of the interfacial energy may lead to interfaces that are still heavily faceted. At intermediate temperatures, both compo-

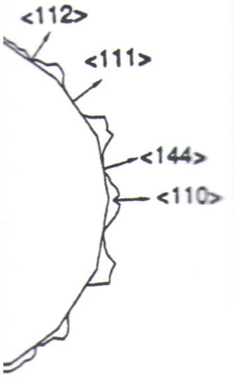

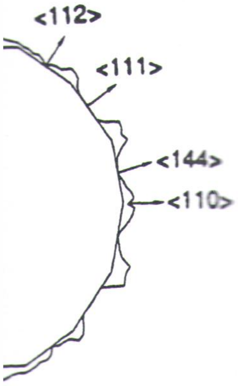

$^{SS}_{c}$ and γ_s^{SS} estimated
9. The plots were nor-

ent at all levels of
or all values of T/T_c
the temperature and
can change appre-
$^{S}/\gamma_s^{SS}$. These results
t interfaces at tem-
$75T_c$ where there is
energy may lead to
tures, both compo-

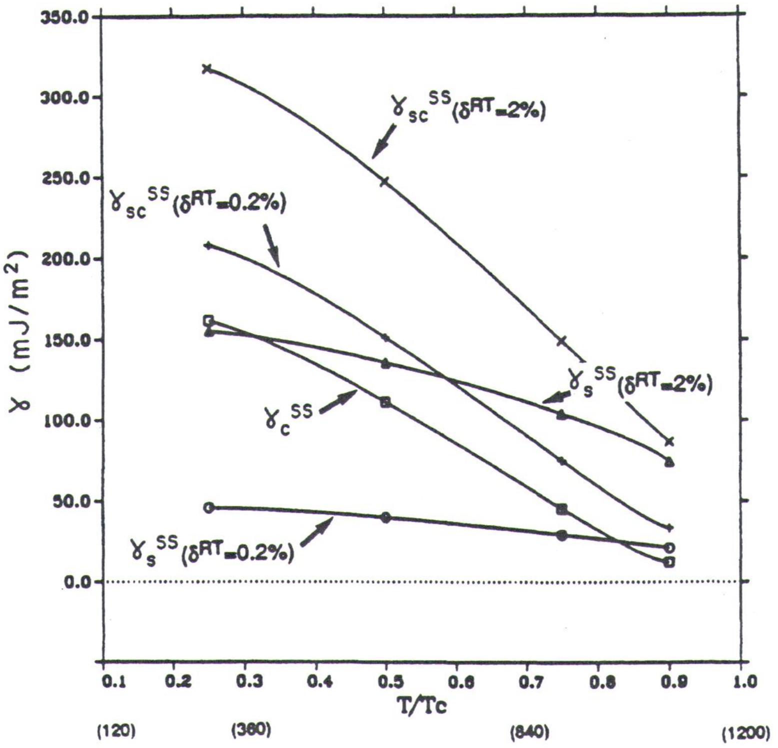

Figure 14.31. The compositional interfacial energy γ_c^{SS} (Eq. 14.27) the van der Merwe structural energy γ_s^{SS} (Eq. 14.39) and the total interfacial energy γ_{sc}^{SS} ($=\gamma_c^{SS}+\gamma_s^{SS}$) of the $\{100\}_{f.c.c.}\|\{100\}_{f.c.c.}$ interface as a function of temperature T/T_c. The absolute temperatures in Kelvin are shown in parentheses. From [130].

nents contribute significantly to the equilibrium shape of the facets at heterophase interfaces.

14.5.5. Atomistic Modeling of Semicoherent Interphase Boundaries

Several detailed calculational and experimental studies have been performed on the structure and energy of semicoherent interphase boundaries in metals [131,132]. The atomistic studies were performed on a number of low-index orientations between two metals using EAM potentials, and the Monte Carlo method was employed to include temperature in some calculations [132]. The predictions of the EAM calculations at 0 K were confirmed experimentally using the rotating crystallite method [22,133]. In this technique, small metal crystals (~ 0.1 μm) deposited on a single-crystal metal substrate are annealed until they rotate into their equilibrium orientation relationship. Some of the more important findings from these studies are summarized below.

Figure 14.32 shows a plot of the interfacial energy γ_{sc}^{SS} versus rotation angle θ for a (001) twist interphase boundary between silver and nickel with a cube-on-cube orientation relationship. This twist interphase boundary is similar to the twist grain boundary shown in Figure 13.10, except that the crystals on either side of the interface are silver and nickel, and because silver and nickel have significantly different lattice parameters ($a_{Ag} = 0.4086$ nm and $a_{Ni} = 0.3524$ nm), there is an orthogonal set of edge-type misfit dislocations present in the interface when $\theta = 0$. This initial dislocation structure then transforms into a set of mixed dislocations with an increasing screw component as θ increases. The elements silver and nickel have a large positive enthalpy of mixing (Table 2.1) and should display very limited mixing across the interface.

Several features are apparent from Figure 14.32. One is that the interfacial energy varies with twist angle, similar to the grain boundaries shown in Figures 13.8 and 13.31. In addition, there is a deep energy minimum at $\theta = 26.56°$ and several shallower minima at other orientations. The deep minimum at $\theta = 26.56°$ corresponds to a $\Sigma = 5/4$ coincidence boundary, as illustrated in Figure 14.33. (The notation 5/4 is the ratio of the inverse density of coincident sites in crystals 1 and 2.) Thus, coincidence boundaries can occur at heterophase interfaces, similar to grain boundaries, and these may be low-energy orientations. This feature is further illustrated by the similarity of Figure 14.33 with Figure 13.11. It is also important to notice that most of the interfacial energies of the silver–nickel (001) twist interface lie between approximately 800 and 900 mJ/m^2 and are on the same order of magnitude as the twist grain boundary energies in Figure 13.31. Thus,

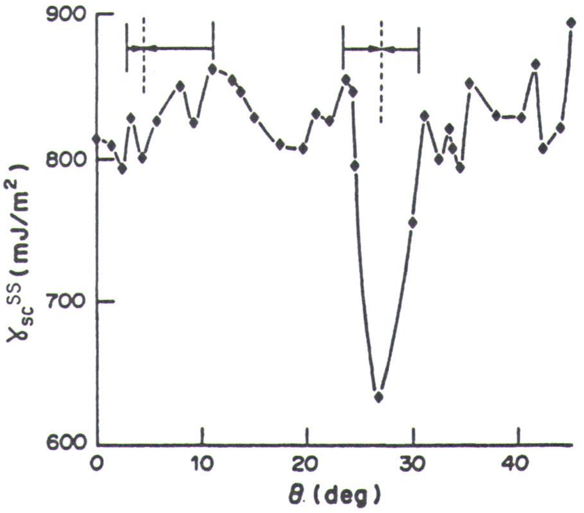

Figure 14.32. Relaxed interfacial energies as a function of twist angle for a (001) semicoherent interface between silver and nickel with a cube-on-cube orientation relationship. Reprinted with permission from [131] by Elsevier Science Ltd., Oxford, England.

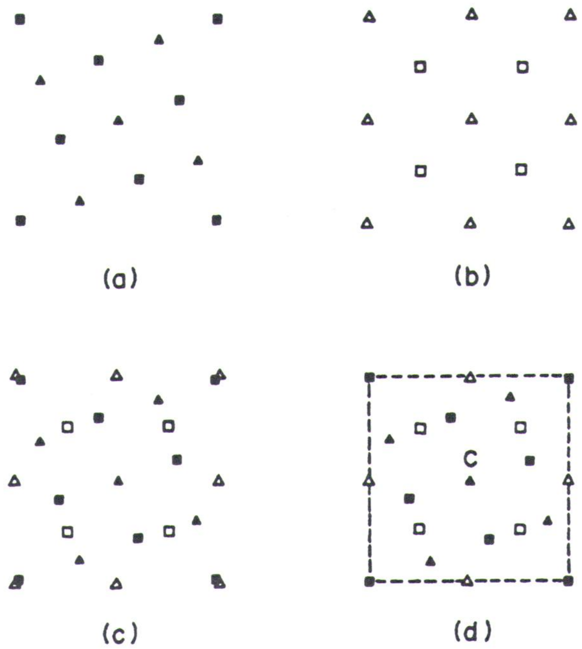

Figure 14.33. Unrelaxed structure for a $\Sigma = 5/4$ (001) twist interphase boundary between silver and nickel. (a) Unit cell of the nickel layer, (b) unit cell of the silver layer, (c) two-dimensional near coincidence structure with a 3.3% misfit between the crystals, and (d) exact coincidence at the interface after uniform deformation to accommodate the misfit. Reprinted with permission from [131] by Elsevier Science Ltd., Oxford, England.

these are fairly high-energy interfaces. Unlike the homophase twist grain boundaries, there is no energy minimum at $\theta = 0°$, because the interphase boundary is still semicoherent.

Gao et al. [131] also examined the detailed atomic relaxations that occurred at the silver–nickel interface as a function of twist angle and found that relaxation occurs in both the silver and nickel crystals. In particular, atoms located at coincidence sites relaxed perpendicular to the boundary but not parallel to it. All other atoms had components of relaxation both parallel and perpendicular to the boundary. These relaxations gave rise to a corrugation of the atomic layers parallel to the interface that extended four to five atomic planes into the crystals. Different degrees of strain localization were observed for the silver and nickel layers because of the different elastic properties of the metals. The misfit dislocation networks always passed midway between the coincident points. The rotating crystallite experiments also performed by these investigators confirmed the presence of a deep energy minimum at $\theta = 26.56°$ in agreement with the interfacial energy calculations.

In a second set of calculations and experiments, Gao et al. [131] determined the interfacial energies of other possible semicoherent interfaces and orientation relationships between silver and nickel crystals. A summary of their results is given in

Table 14.3. The most important features of these low-index interfaces are listed below.

1. The lowest interfacial energy is found for the $(111)_{Ag}\|(111)_{Ni}$ interface with $\theta = 0°$ (i.e., with parallel close-packed atomic rows), and the second lowest occurs for the $(111)_{Ag}\|(001)_{Ni}$ interface with parallel close-packed atomic rows.
2. The interfaces with parallel close-packed atomic rows (i.e., with $\theta = 0°$) are always energetically favored except for the $(111)_{Ag}\|(110)_{Ni}$ interface.
3. The interfaces formed by joining low-energy solid–vapor surfaces, for example, the (111) planes, are associated with low interfacial energies.
4. Inverting the crystals at the interface, for example, changing the $(111)_{Ag}\|(001)_{Ni}$ interface to the $(111)_{Ni}\|(001)_{Ag}$ interface, changes the energy.

These results are entirely consistent with the interfacial behavior discussed for epitaxial films in Section 7.2 and grain boundaries in Section 13.2.4, further emphasizing the importance of nearest-neighbor bonding in determining the orientation relationships and interfacial energies at interfaces. Notice that the interfacial energy of the $(111)_{Ag}\|(111)_{Ni}$ interface (417 mJ/m^2) is approximately half that of the other interfaces. Crystallite rotation experiments performed for silver droplets on nickel substrates confirmed the predictions of the EAM calculations in these orientations shown in Table 14.3. The atomic relaxations at these interfaces are examined in detail by Gao et al. [131], and they are not discussed here.

Lastly, we mention EAM Monte Carlo calculations that were used to examine the structure and properties of a semicoherent copper–silver (001) interphase boundary with the crystals in a cube-on-cube orientation relationship [132]. This interface is interesting because copper and silver display mutual solid solubility with temperature, and, therefore, there should be some compositional mixing at the interface superimposed on the dislocation network necessary to accommodate misfit between the crystals. This is observed in the calculations, as illustrated in Figure 14.34. In this figure, it can be seen that the width of the composition profile associated with the interface increases with increasing temperature in the range of 600 to 900 K, in accordance with the predictions of both the continuum and discrete lattice plane models of coherent interfaces (Section 14.2). In contrast to the profile of a perfectly coherent interface (Fig. 14.3), the composition profile of the semicoherent

Table 14.3. Calculated interfacial energies of various low-index silver–nickel interfaces

	Ag (001)		Ag (110)		Ag (111)	
Ni	0°	90°	0°	90°	0°	90°
(001)	814	814	1124	1124	437	437
(110)	995	995	828	1214	988	718
(111)	670	670	670	960	416	468

Source: From [131].

faces are listed be-
)$_{Ni}$ interface with θ
: second lowest oc-
icked atomic rows.
:, with $\theta = 0°$) are
; interface.
surfaces, for exam-
ergies.
le, changing the
changes the energy.

: discussed for epi-
, further emphasiz-
he orientation rela-
nterfacial energy of
hat of the other in-
droplets on nickel
1 these orientations
re examined in de-

re used to examine
r (001) interphase
ship [132]. This in-
olid solubility with
mixing at the inter-
nmodate misfit be-
lustrated in Figure
ition profile associ-
the range of 600 to
and discrete lattice
to the profile of a
of the semicoherent

er–nickel interfaces

Ag (111)	
0°	90°
437	437
988	718
416	468

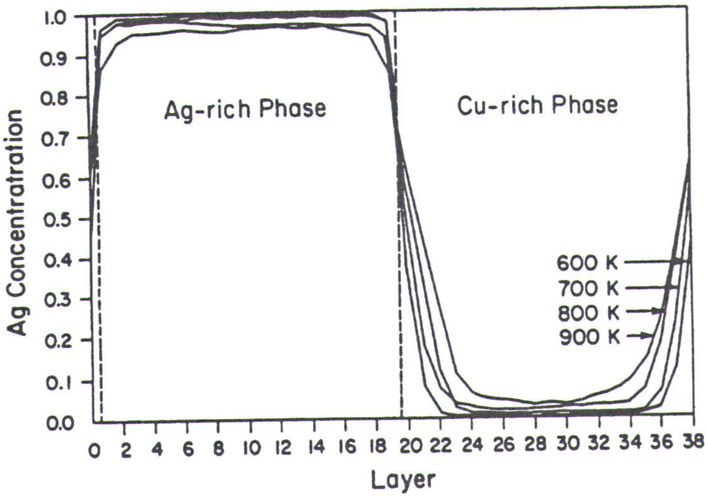

Figure 14.34. Silver concentration in each atomic layer as a function of layer number, for four different temperatures. The vertical dashed lines represent the locations of the physical interfaces, where the number of atoms per layer changes from that appropriate to a copper-rich slab to that of a silver-rich slab. Reprinted with permission from [132] by Elsevier Science Ltd., Oxford, England.

interface is asymmetric in Figure 14.34. This interface is associated with a Gibbsian excess of silver if the position of the dividing surface is chosen at the physical interface. As in many of the EAM studies discussed before, detailed examination of the atomic positions revealed that the distribution of silver and copper in the layers was not uniform, with the larger silver atoms tending to cluster in regions of tension at the interface and the smaller copper atoms in regions of compression. It was also observed that the interfacial dislocations were localized and symmetrical at 600 K, but that they tended to wander with increasing temperature and appeared to loose their identify between 800 and 900 K, possibly indicating the transition to an incoherent interface in that temperature range. The overall features of this interface are similar to those revealed by the regular solution calculation discussed in Section 14.5.4.

14.6. INTERFACES BETWEEN PHASES WITH DIFFERENT BRAVAIS LATTICES

In Sections 14.2 and 14.5, we considered coherent and semicoherent interfaces between two phases with the same crystal structure but different compositions. The phases also had the same orientation, often referred to as a parallel or cube-on-cube orientation relationship. Many heterophase interfaces form between two phases with different Bravais lattices, and we need to understand the behavior of these types of interfaces. These are the most complicated interfaces, but we will see that they display similar behavior in an attempt to minimize the interphase boundary energy. As before, we limit our discussion to metal–metal interfaces, but it is important to realize that the same principles and behavior apply to other heterophase interfaces, such as metal–ceramic [3,22], ceramic–polymer [4] and semiconductor–semiconductor [5] materials.

14.6.1. Orientation Relationships at Heterophase Interfaces

In Section 7.2.4, we showed that there was a strong tendency for a thin film of one crystal structure on a substrate with a different crystal structure to align such that their close-packed planes and directions were parallel. This was referred to as atomic row matching [20] and the same phenomenon occurs for heterophase interfaces between two semiinfinite crystals with different structures. In the case of a martensitic transformation the two phases may have the same composition but different crystal structures, such as the f.c.c.–h.c.p. interface in a cobalt–nickel alloy, as shown in Figure 12.4, for example; however, in a diffusional transformation, the phases may vary both in structure and composition, as illustrated by a similar f.c.c.–h.c.p. interface in an aluminum–silver alloy (Fig. 14.35). In both of these figures, the viewing direction is $[10\bar{1}]_{\text{f.c.c.}}\|[11\bar{2}0]_{\text{h.c.p.}}$ and the orientation relationship between the two phases is

$$(111)_{\text{f.c.c.}}\|(0001)_{\text{h.c.p.}};\ [10\bar{1}]_{\text{f.c.c.}}\|[11\bar{2}0]_{\text{h.c.p.}}. \tag{14.44a}$$

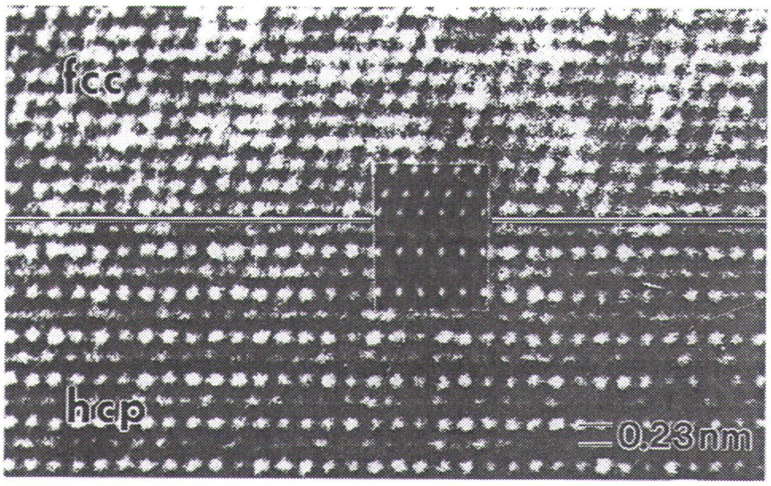

Figure 14.35. Experimental HRTEM image of a γ' (Ag_2Al) precipitate interface in an aluminum–silver alloy with a superimposed simulated image of the interface. The position of the interface between the f.c.c. and h.c.p. phases is indicated by a line. From [23] copyright Taylor & Francis Ltd.

This is the so-called Shoji-Nishiyama (SN) orientation relationship [134], and the parallel close-packed planes are edge-on and horizontal in Figure 14.35. Note that the interface plane (often called the habit plane when referring to plate or lath-shaped precipitates) is the parallel close-packed planes in the two structures. The lattice parameters are such that the hexagonal arrangement of atoms in the $\{111\}$ and (0001) close-packed planes of the phases in Figures 12.4 and 14.35 match almost perfectly and large coherent interfaces are formed. In this case, there are no nearest-neighbor broken bonds across the interface, only bonds that have a compositional difference, as in Figure 14.35, or a stacking difference (Section 13.2.5), as in Figure 12.4. Consequently, these are expected to be low-energy interfaces with interfacial energies of approximately 15 and 30 mJ/m^2, respectively, at room temperature [135,136].

As in the f.c.c.–h.c.p. example above, relatively good atomic matching occurs between the close-packed planes of b.c.c. phases and the f.c.c. and h.c.p. phases. The f.c.c.–b.c.c. case was illustrated previously in Figure 7.10 and a similar figure can be constructed for a b.c.c.–h.c.p. interface. This leads to two other well-known orientation relationships, which are similar to Eq. (14.44a) called the Kurdjumov–Sachs (KS) [137] orientation relationship

$$(111)_{\text{f.c.c.}}\|(110)_{\text{b.c.c.}};\ [0\bar{1}1]_{\text{f.c.c.}}\|[1\bar{1}1]_{\text{b.c.c.}}, \tag{14.44b}$$

where the close-packed planes and direction in the f.c.c. and b.c.c. phases are parallel, and the Burgers [138] orientation relationship

$$(110)_{\text{b.c.c.}}\|(0001)_{\text{h.c.p.}};\ [1\bar{1}1]_{\text{b.c.c.}}\|[11\bar{2}0]_{\text{h.c.p.}}, \tag{14.44c}$$

where the close-packed planes and directions of the b.c.c. and h.c.p. phases are parallel. Another common orientation relationship is the Nishiyama-Wasserman (NW) orientation relationship [139,140], where the close-packed directions in the f.c.c. and b.c.c. phases are rotated out of alignment by 5.26° so that $[011]_{\text{f.c.c.}}\|[001]_{\text{b.c.c.}}$ (as shown in Fig. 7.10a). A similar rotated situation in the b.c.c.–h.c.p. system where $[110]_{\text{b.c.c.}}\|[01\bar{1}0]_{\text{h.c.p.}}$ is called the Pitsch–Schrader orientation relationship [141]. These and other orientation relationships commonly found in f.c.c.–b.c.c.–h.c.p. systems have been analyzed by Dahmen [20]. They are expressed according to Eq. (13.8).

It is important to note that the basic arrangement of atoms in the close-packed planes of f.c.c., b.c.c. and h.c.p. crystals (e.g., in Fig. 7.10) is a rhombus and that aligning the close-packed planes in the crystals across the interface is equivalent to matching the rhombohedral symmetries of the atomic arrangements of the low-energy close-packed planes in the structures [20,142,143]. Aligning particular rows of atoms in these planes (row matching) further reduces the energy of the interfaces. This feature has been demonstrated in energetic calculations by van der Merwe [142] and others [144–146], which show that the orientation relationships above minimize the elastic strain energy of the interfaces. An example of such data was previously shown in Figure 7.11 for the $(111)_{\text{f.c.c.}}\|(110)_{\text{b.c.c.}}$ interface. Thus, the interfacial energy of most heterophase interfaces is minimized through atomic row-matching, and this criterion usually determines the equilibrium orientation relationship between two different phases.

Dahmen [20] has shown that the rows of atoms that superimpose between the two crystals in Figure 7.10b can be viewed as an invariant line between the two structures. In a continuum sense, an invariant line is a direction that is both undistorted and unrotated when one crystal structure transforms into another. This is illustrated schematically in Figure 14.36. In Figures 7.10a and 14.36a, we imagine that a unit cell of the b.c.c. lattice (open circles) is transformed into a unit cell of the f.c.c. lattice (filled circles) by an expansion $e_{22}(\mathrm{b})$ along the y direction and a contraction $e_{11}(\mathrm{a})$ along the x direction. This defines both the lattice correspondence and the transformation strain. The two axes x and y are the principal axes of the transformation and this operation may be written as a diagonal matrix

$$\mathbf{A} = \begin{bmatrix} e_{11} & 0 \\ 0 & e_{22} \end{bmatrix} \tag{14.45}$$

when related to the principal coordinate system. The length of a vector $\mathbf{u}$ will change to $|\mathbf{v}| = |\mathbf{Au}|$ during the transformation. This is the well-known description of the deformation of a circle ($u_x^2 + u_y^2 = 1$) into an ellipse ($v_x^2/\mathrm{a} + v_y^2/\mathrm{b} = 1$) with major axes a and b. An illustration of the continuum deformation corresponding to Figure 7.10a is shown in Figure 14.36, where the circle represents the b.c.c. plane and the ellipse the f.c.c. plane. Any radius vector on the circle will change both length and direction during the transformation. A special vector is the one ending at **C** because it changes direction from **C** to **C**′ but its length is preserved. If the directional change from **C** to **C**′ is compensated by a rigid-body rotation of the transformed structure (ellipse) it will become an invariant line (i.e., an undistorted and unrotated

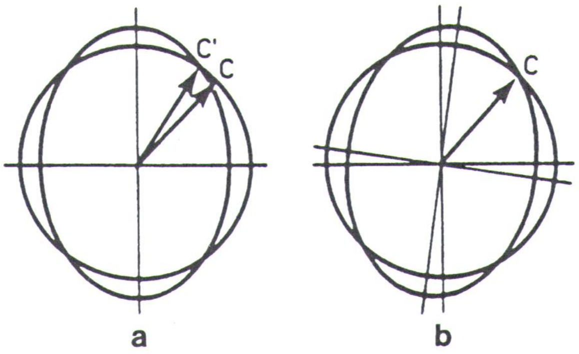

Figure 14.36. The lattice strain of Figure 7.10 in continuum representation. (a) The circle (b.c.c. plane) is transformed into an ellipse (f.c.c. or h.c.p. plane). (b) A small rotation bringing **C** and **C**′ into coincidence produces an invariant line. Reprinted with permission from [20] by Elsevier Science Ltd., Oxford, England.

direction during the transformation). In terms of matrix notation, the total deformation in Figure 14.36b can be decomposed into the shape deformation **A** and a rigid-body rotation **R**, or **RA**. Because the rows of atoms along the $[011]_{\text{f.c.c.}}\|[111]_{\text{b.c.c.}}$ direction in Figure 7.10b exactly superimpose, they satisfy this criterion (i.e., they form an invariant line on an atomic level).

Due to the special choice of lattice parameters in Figure 7.10b, the invariant line coincides with the low-index close-packed direction. This is not usually the case, and in general the invariant line is a nonrational direction. Dahmen [20] has used matrix algebra to find the angle of rotation that is necessary to form an invariant line as a function of the ratio of the principal distortions $e_{11}(\mathfrak{a})$ and $e_{22}(\mathfrak{b})$. Because e_{11} and e_{22} have a constant ratio for a given f.c.c.–b.c.c. or h.c.p.–b.c.c. transformation, the angle θ simply becomes a function of the lattice parameter ratios $\mathfrak{r} = \mathfrak{a}_{\text{f.c.c.}}/\mathfrak{a}_{\text{b.c.c.}}$ or $\sqrt{2}\mathfrak{a}_{\text{h.c.p.}}/\mathfrak{a}_{\text{b.c.c.}}$. This function is shown in Figure 14.37, where it can be seen that θ varies rapidly from 0° at the exact NW orientation relationship for $\mathfrak{r} < 1/\sqrt{2}$ and $\mathfrak{r} > \sqrt{3}/2$ to a wide maximum at the exact KS orientation relationship at 5.26° for $3/4 < \mathfrak{r} < \sqrt{6}/3$. Thus, the NW and KS orientation relationships cover most of the possible rotations between the close-packed planes, which is why they are the dominant orientation relationships found experimentally [20,147]. The energetic calculations by van der Merwe [142] show that the NW and KS orientations are also the lowest energy orientations. Thus, the geometrical analysis of Dahmen agrees with the energetic calculations of van der Merwe and others. It has been shown that the formation of an invariant line as described above is exactly analogous to forming O-lines in the interface (Fig. 13.17) and that the same result can be obtained by either theory [148–150].

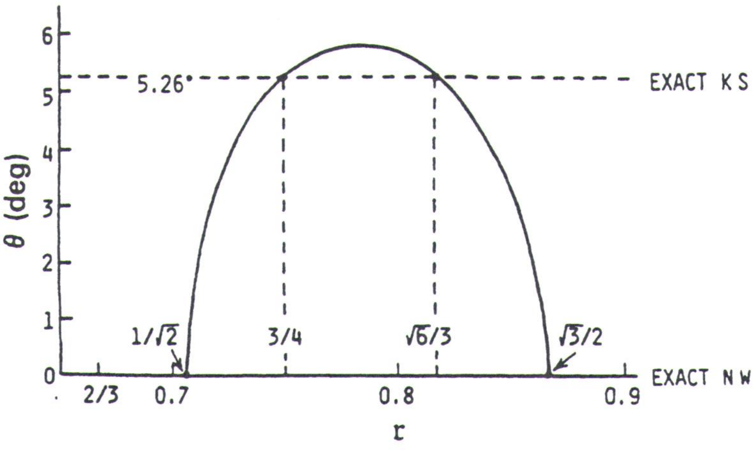

Figure 14.37. Rotation angle θ necessary to produce an invariant line by rotation around the normal to the close-packed planes as a function of the lattice parameter ratio $\mathfrak{r}$. From [20,147] reprinted with kind permission from Elsevier Science S. A., Lausanna, Switzerland.

14.6.2. High-Index Heterophase Interfaces

It is possible to have a fully coherent f.c.c.–h.c.p. interface if the atomic sizes are similar in the two phases, as in the aluminum-silver system shown in Figure 14.35. In contrast, even if the atom sizes are the same, it is not possible to have fully coherent f.c.c.–b.c.c. and h.c.p.–b.c.c. heterophase interfaces because the sixfold symmetries of the close-packed $\{111\}_{\text{f.c.c.}}$ and $(0001)_{\text{h.c.p.}}$ planes do not match the twofold symmetry of the $\{110\}_{\text{b.c.c.}}$ plane. Hence, these interfaces must be semicoherent in some directions. This feature is illustrated schematically in Figure 14.38, where the lattice parameter ratio has been adjusted so that the rhombohedral patterns of atoms in the f.c.c. (filled circles) and b.c.c. (open circles) have exactly the same spacing along the y direction (i.e., $r = a_{\text{f.c.c.}}/a_{\text{b.c.c.}} = 1.15$). This produces atomic row matching parallel to the x direction as indicated by the heavy dashed line. Normal to this direction are rows of perfectly matched atoms (invariant lines or O-lines) with complete disregistry in between. The regions of disregistry correspond to edge misfit dislocations in the interface, parallel to the invariant line. This situation is analogous to the semicoherent interfaces shown in Figures 13.18d and 14.24, except that the phases on either side of the interface have different lattices. We now show that it is possible to transform this semicoherent interface into a fully coherent interface by rotating the interface plane so that it is no longer parallel to the common close-packed planes.

Figure 14.39 shows four different interfacial structures that could form between two crystals that are related by a transformation strain that includes a simple shear e_{12} and an expansion e_{11} in the shear plane so that the transformation matrix [151,152] can be written as

$$\mathbf{A} = \begin{bmatrix} e_{11} & e_{12} \\ 0 & 1 \end{bmatrix}. \tag{14.46}$$

This deformation changes a square (top crystal in Fig. 14.39) into a rhombus (bottom crystal in Fig. 14.39) and leaves the spacing of the planes normal to the direction of the shear equal. This type of deformation is appropriate to the f.c.c.→b.c.c. transformation and in fact, the lines that form the square lattice in Figure 14.39 can be imagined to be the $\{110\}$ planes of the b.c.c. phase and the set of lines that form the rhombus in the opposite crystal can be imagined as the $\{111\}$ planes of the f.c.c. phase [55,152]. Thus, this schematic represents a fairly general f.c.c.–b.c.c. interface.

Figure 14.39a shows the interface parallel to the shear plane (the parallel $\{111\}_{\text{f.c.c.}}$ and $\{110\}_{\text{b.c.c.}}$ planes), with the misfit in this plane accommodated by an array of $a/2\langle 110\rangle$ lattice dislocations in the square (b.c.c.) lattice. This interface is analogous to that in Figure 14.38. In Figure 14.39b, the interface plane has been rotated through an angle θ that is related to the shear strain e_{12} and the dilatational strain e_{11} [151–153] by

$$\tan\theta = e_{11}/e_{12}. \tag{14.47}$$

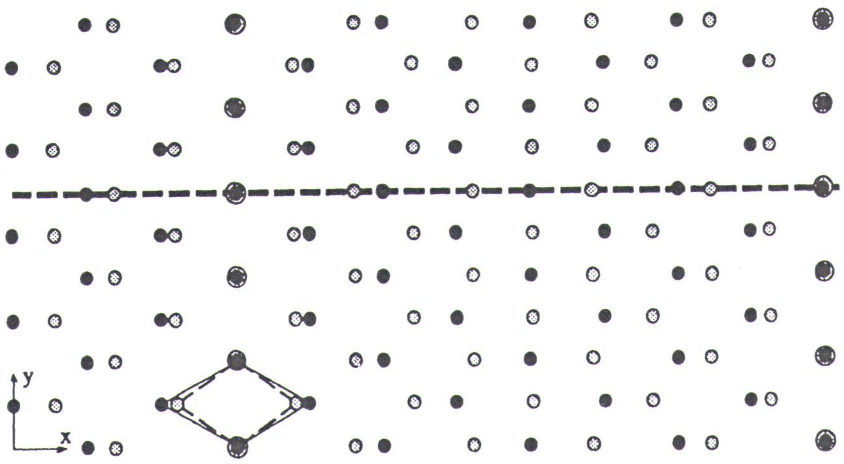

Figure 14.38. Schematic diagram representing the rhombic surface unit cells of a {111} f.c.c. plane (filled circles) and a {110} b.c.c. plane (open circles) when $\tau = a_{\text{f.c.c.}}/a_{\text{b.c.c.}} = 1.15$. From [143].

This produces an interface along a high-index direction **u**, which is an undistorted and unrotated direction in the two crystals (i.e., it is an invariant line). If this invariant line is resolved onto every other close-packed plane, the staggered array of ledges shown in Figure 4.91c is formed. This type of interface corresponds to the f.c.c.→h.c.p. transformation, which is discussed further in the following section on the TLK structure of heterophase interfaces. In the f.c.c.→h.c.p. case, each ledge is bounded by an $a/6\langle 112\rangle$ partial dislocation, which accomplishes the structural part of the transformation. If instead, the invariant line is resolved onto every close-packed plane, the staggered array in Figure 14.39d results. This is the case of an f.c.c.→b.c.c. transformation interface with every ledge bounded by an $a/12\langle 112\rangle$ partial dislocation [17]. An example of such an interface is shown in Figure 12.7 (also shown enlarged in Problem 14.23).

In the area of diffusional transformations, the ledges in Figure 14.39d are often called structural ledges because they are considered an intrinsic part of the interfacial structure [55,56]. Experimental evidence suggests that they are relatively immobile and that growth occurs locally at larger ledges or perturbations which move along the interface [154]. In martensitic transformations, such ledges are highly mobile and accomplish the required structural transformation [1,17]. Thus, they are often called transformation dislocation ledges. It is important to note that all of the linear defects shown in Figure 14.39 can be characterized according to their dislocation and ledge contents within the DSC framework discussed in Section 13.23 and illustrated, for example, in Figures 13.24 and 13.25. Crystallographically, the ledges illustrated in Figure 14.39d are identical in martensitic and diffusional transformations, although their kinetic behavior may be different in the two types of transformation.

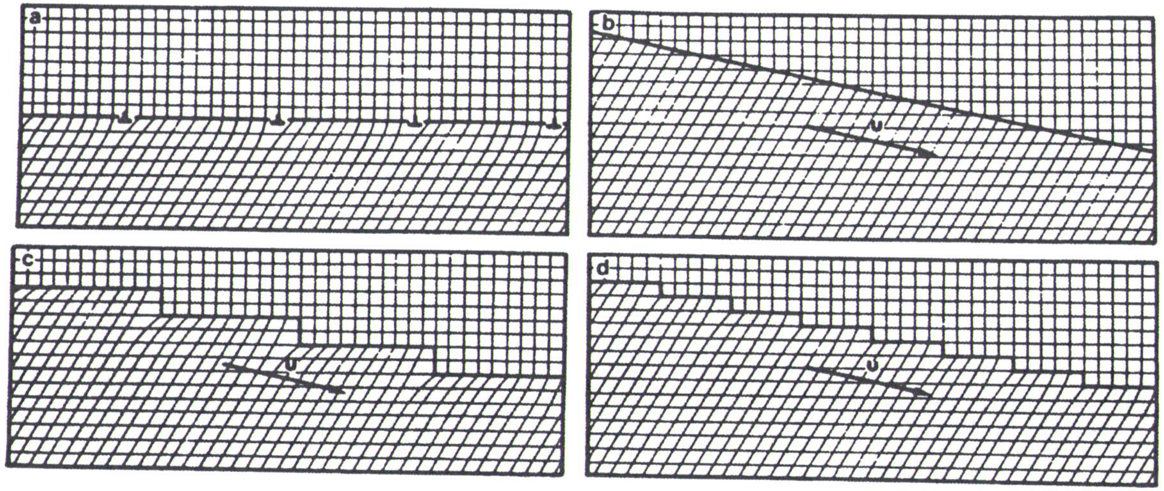

Figure 14.39. Possible interfaces for a transformation described by a shear e_{12} coupled with an expansion e_{11} in the shear plane. (a) The expansion is accommodated by a set of perfect lattice (misfit) dislocations. (b) The interface lies along an invariant line **u** and no dislocations are necessary. (c) The invariant line is resolved onto every other close-packed plane as in the f.c.c.–h.c.p. transformation where each ledge is an $a/6<112>$ partial dislocation. (d) The invariant line is resolved onto every close-packed plane as in an f.c.c.–b.c.c. transformation where each ledge contains an $a/12<112>$ partial dislocation. Reprinted with permission from [153] by Elsevier Science Ltd., Oxford, England.

The interface in Figure 14.39 is only a two-dimensional sketch, and the behavior of the crystals in the third dimension has been omitted for clarity. In many interfaces, there is additional misfit in the third dimension, which can be accommodated by another set of misfit dislocations in the interface parallel to the invariant line **u** as illustrated in Figure 14.40a. Alternatively, these dislocations can be transformed into a second set of ledges on the close-packed planes perpendicular to the first set that produces a second high-index direction **v** in the interface, as illustrated in Figure 14.40b.

Still more complicated situations can be envisioned and are often found at heterophase interfaces in materials. For example, suppose that, in addition to the

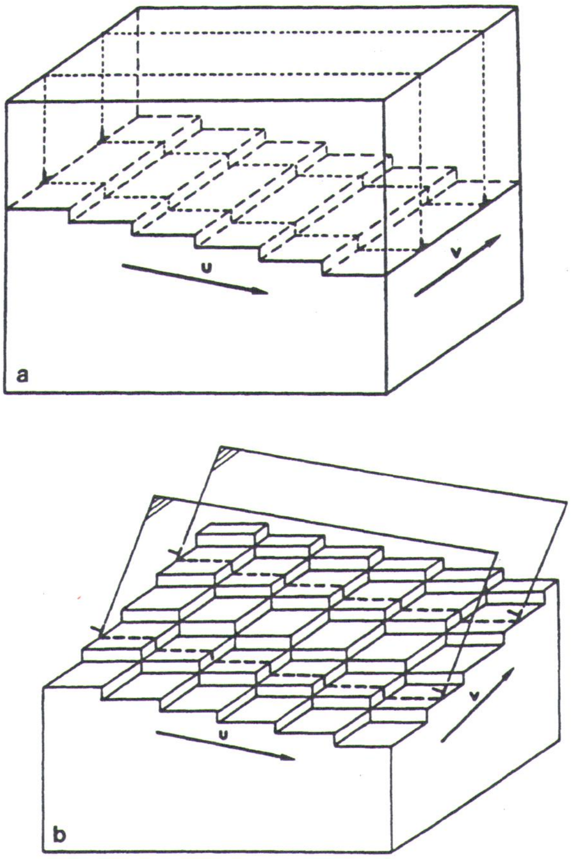

Figure 14.40. (a) The interface in Figure 14.39d in perspective with the crystal lattices omitted for clarity. Additional misfit in the direction **v** is accommodated by a set of lattice misfit dislocations similar to those in Figure 14.39a. (b) A geometrically glissile invariant plane strain interface as in a martensite transformation. The direction **v** is now high-index and an additional simple shear is accommodated by a set of dislocations which are glissile in the interface. Reprinted with permission from [153] by Elsevier Science Ltd., Oxford, England.

shear and dilatation in Figure 14.40, there is a dilatation (misfit) normal to the plane of the shear so that the close-packed planes that are parallel to the interface in Figure 14.39a no longer have the same interplanar spacing. This misfit can be accommodated in one of two ways: (a) by inserting misfit dislocations periodically along the interface [55,143] (as illustrated in Fig. 14.41), or (b) by partitioning the strain evenly among all the ledges in Figure 14.39d, which is equivalent to performing a small rigid-body rotation between the two crystals about an axis that is normal to the plane of the figure similar to that shown in Figure 14.36 [155]. Both cases have been observed experimentally, but one partitions the misfit evenly along the surface, whereas the other localizes it into misfit dislocations.

Figure 14.39 showed schematically how a semicoherent planar interface between two crystals could transform into a coherent ledged interface containing an invariant line by rotation of the interface plane. The energetics of this process have been calculated by van der Merwe et al. [56] and shown to be favorable for small misfits and large pattern advances when the interface is stepped. The idea of pattern advance created by a stepped (ledged) interface is illustrated in Figure 14.42. Figure 14.42a shows an invariant line formed between two crystals and is similar to Figure 14.39b. In Figure 14.42b, the same interface is shown on an atomic level where ledges spaced periodically along the interface are evident. Notice that when crystal *B* steps down one plane parallel to the interface at a ledge, a pattern of the lattice a distance of $\delta\mathfrak{b}_{[100]}$ advances to the left, as indicated in the figure. According to theory [56], the center-to-center distance of consecutive terraces $D_{\alpha[100]}$ along the [100] direction in the close-packed plane is given as

$$D_{\alpha[100]} = \frac{-\delta\mathfrak{b}_{[100]}}{\mathfrak{b}_{[100]} - 1}, \tag{14.48}$$

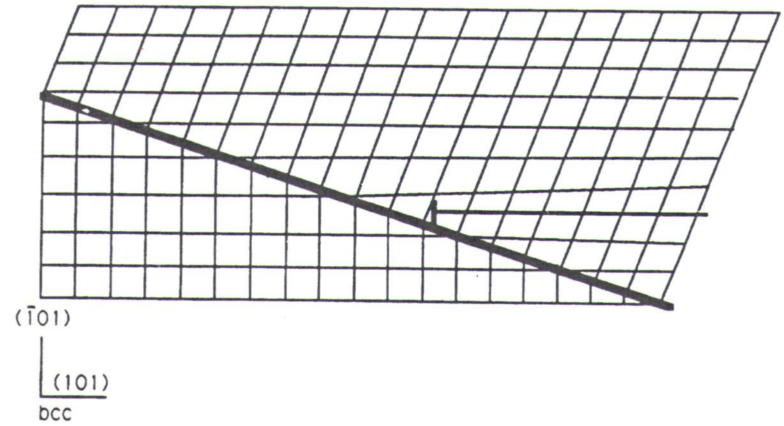

Figure 14.41. Illustration of additional misfit normal to the close-packed planes in Figure 14.39b accommodated by a misfit dislocation with a Burgers vector inclined to the invariant line. Reprinted with permission from [152] by Elsevier Science Ltd., Oxford, England.

) normal to the plane
the interface in Fig-
isfit can be accom-
s periodically along
artitioning the strain
lent to performing a
xis that is normal to
55]. Both cases have
venly along the sur-

planar interface be-
erface containing an
of this process have
favorable for small
. The idea of pattern
Figure 14.42. Figure
l is similar to Figure
atomic level where
ce that when crystal
ttern of the lattice a
. According to theo-
$_{[100]}$ along the [100]

(14.48)

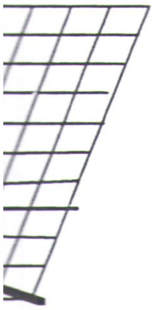

cked planes in Figure
nclined to the invariant
ord, England.

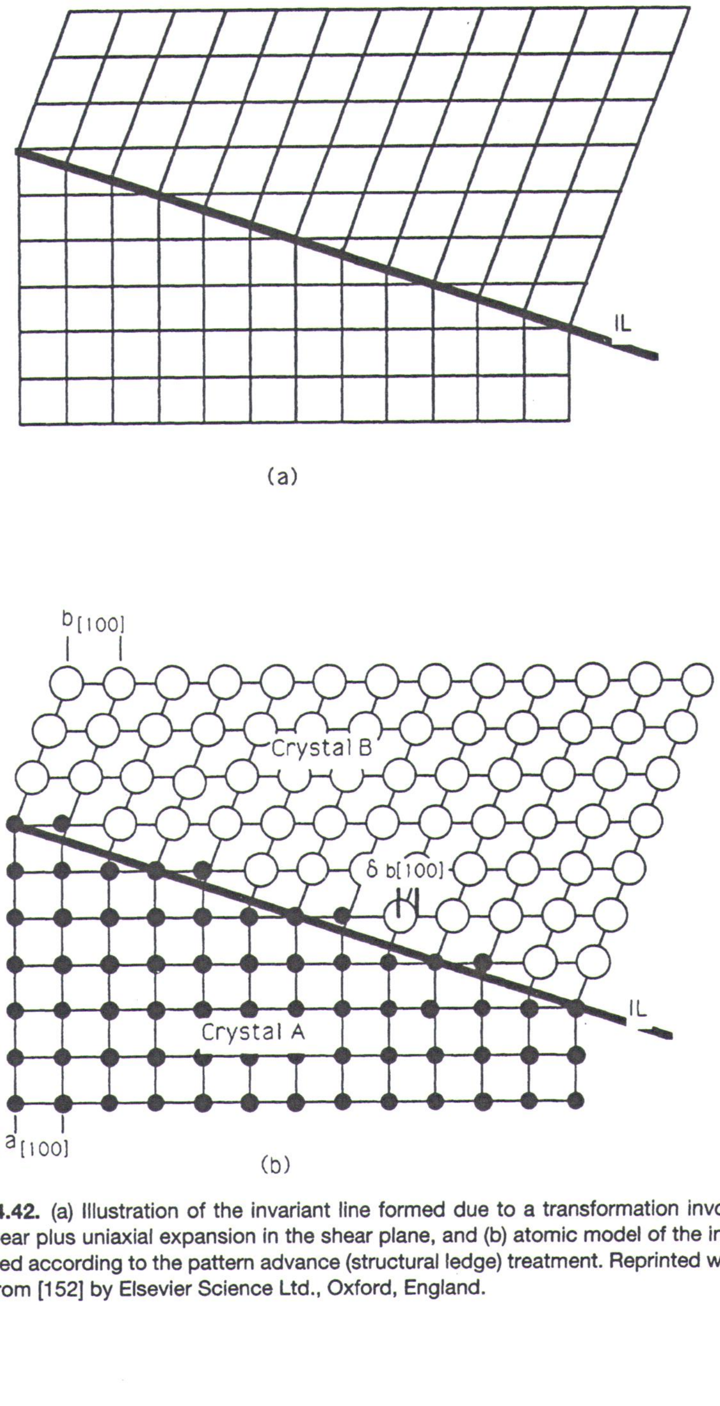

Figure 14.42. (a) Illustration of the invariant line formed due to a transformation involving a simple shear plus uniaxial expansion in the shear plane, and (b) atomic model of the interface constructed according to the pattern advance (structural ledge) treatment. Reprinted with permission from [152] by Elsevier Science Ltd., Oxford, England.

where $\delta\mathfrak{b}_{[100]}$ is the forward displacement of the B atomic ledge and $\mathfrak{b}_{[100]}$ is the lattice spacing of the B crystal along the [100] direction, as indicated in Figure 14.42b. The angle between [100] and the habit plane is then given by

$$\tan\theta = \frac{\mathfrak{a}_{\perp}}{D_{\mathfrak{a}[100]}}, \tag{14.49}$$

where $\mathfrak{a}_{\perp}$ is the lattice spacing normal to the parallel close-packed planes. Equation (14.49) produces a result identical to Eq. (14.47) for the transformation strain in Eq. (14.46), but now based on atomic pattern matching across the interface. This approach to interfacial structure has been highly developed [56,143] and compared with the invariant line theory [149,152], and can be useful for analyzing high-index ledged interfacial structures [43,155].

To illustrate the use of the invariant-line and structural-ledge treatments, consider the interface shown in Figure 14.42. Crystal B is produced from crystal A by a simple shear $e_{12} = 0.34$ accompanied by a 10% expansion in the (001) shear plane such that $e_{11} = 1.1$. The corresponding transformation matrix (Eq. 14.46) is

$$\mathbf{A} = \begin{bmatrix} 1.1 & 0.34 \\ 0 & 1 \end{bmatrix}.$$

When these values are substituted into Eq. (14.47), the angle between the [100] direction and the invariant line is given by $\theta = 16.7°$. The resulting interface between the two lattices is shown in Figure 14.42a. According to the structural-ledge treatment, the center-to-center distance between consecutive (001) terraces along the [100] direction is given by Eq. (14.48) as

$$D_{\mathfrak{a}[100]} = \frac{0.34}{1.1 - 1} = 3.34$$

or 3.34 $(100)_A$ lattice planes. The angle between the [100] direction and the habit plane is then given by $\theta = \tan^{-1}(1/3.34) = 16.7°$, which is identical to the answer above for the invariant-line theory. This interface is shown in Figure 14.42b. In this calculation, we used the transformation matrix **A** to determine the orientation of the habit plane according to Eqs. (14.48) and (14.49). It is also possible to determine the habit plane based on the relative displacements of atomic patterns in two phases across an interface [56]. This method was used to analyze the formation of the $\{474\}_{\gamma}$ habit plane shown in Figure 12.7 and the reader may consult [16] for an example calculation.

In closing this section, it is important to mention that a number of different approaches to predicting and analyzing heterophase interfaces have been proposed and utilized with various degrees of success. These include the O-lattice, CSL and DSC theories discussed in Sections 13.2.2 and 13.2.3., the invariant-line and pattern-matching theories just mentioned, as well as the phenomenological theory of martensite crystallography [1,156,157]. We have used several of these in the analyses above and a number are compared in the literature [16,42,52,58,127,149,152]. Each approach has its own strengths and weaknesses, requires certain input, and most yield similar if not identical results. The reader should consult these references for more detailed descriptions of the various theories on solid–solid interphase boundary structures.

It is also important to note that all of the energetic calculations performed for the ledged interfaces described above only included the structural (elastic) energy contribution (γ_s^{SS}) to the interphase boundary energy. Calculations that include the compositional contribution (γ_c^{SS}) of wrong compositional bonds across ledged interphase boundaries, such as those in Figures 12.7 and 14.39d, are just beginning to be performed; these are discussed in the following section.

14.6.3. Atomistic Calculations

Atomistic calculations of the interfacial properties of high-index interfaces between crystals that have a well-defined orientation relationship but different Bravais lattices and compositions are just beginning to be performed. So far, all of the calculations have been performed for f.c.c.–b.c.c. interfaces similar to those shown in Figures 12.7 and 14.42, because this represents an important and fairly common type of interface. Some of the results from atomistic calculations of the high-index interfaces are summarized below.

Figure 14.43a shows an atomistic model of a high-index f.c.c.–b.c.c. interface. The interface was constructed using a NW orientation relationship between the phases and an EAM iron potential (e.g., appropriate for an f.c.c.–b.c.c. martensite interface). Approximate interfacial energies were obtained with fully relaxed simulation conditions for interfaces with orientations that varied from 0 to 26° with respect to the parallel close-packed $(111)_{\text{f.c.c.}} \| (110)_{\text{b.c.c.}}$ planes. The calculations showed that an interface with monatomic ledges, inclined about 13° with respect to the parallel close-packed planes, yielded the lowest interfacial energy with a value of about 240 mJ/m^2. This interface is shown in Figure 14.43b, and it is the maximum coherency interface observed experimentally [158]. A similar calculation for a $(121)_{\text{f.c.c.}}$ interface between f.c.c. and b.c.c. iron phases with a KS orientation relationship yielded an interphase boundary energy of 179 mJ/m^2 [100]. Both of these interfacial energies are considerably lower than the energies of the semicoherent interfaces modeled using the EAM potentials in Section 14.5.5., indicating that it is energetically favorable for semicoherent interfaces to form coherent ledged interfaces, as illustrated schematically in Figure 14.39.

The most recent study of this type was performed for a $(121)_{\text{f.c.c.}}$ interface between nickel and chromium crystals (and alloys) in a KS orientation relationship using EAM potentials [102]. A projection of the atomic structure of this interface for pure nickel and chromium is shown in Figure 14.44. This study is particularly interesting because f.c.c. nickel can accommodate up to almost 50 at.% chromium (the heat of mixing is approximately 0.06 eV/atom) and, therefore, it is possible to examine the interfacial structure and energy as a function of chromium concentration in the f.c.c. phase. It was found that the interfacial energy varies only slightly with

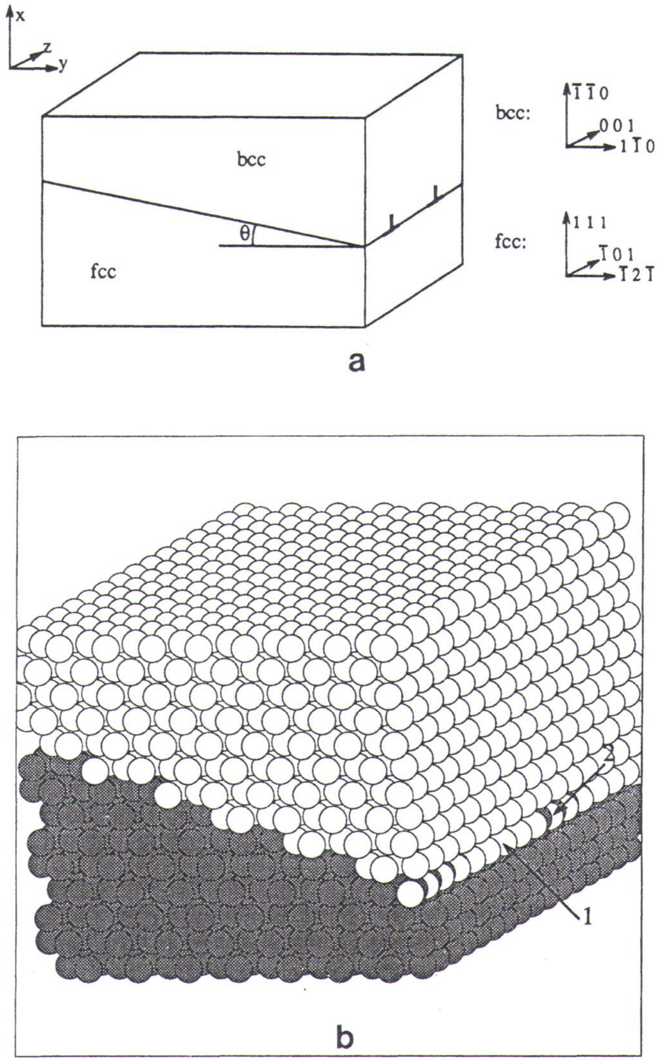

Figure 14.43. (a) Schematic drawing of an f.c.c.–b.c.c. interface with the NW orientation relationship, and (b) atomic model of the interface with $\theta = 13°$ with respect to the close-packed planes. The numbers 1 and 2 in (b) indicate coherent regions and misfit dislocations in the interface, respectively. From [100].

chromium concentration, decreasing from 216 to 200 mJ/m^2 as the chromium concentration increases from 0 to 50 at.%. Because this value is close to the value of 179 mJ/m^2 found for the same $(121)_{\text{f.c.c.}}$ interface with an iron potential above, and it does not vary more than 10% with composition, these results indicate that the major portion of the interfacial energy (80% to 90%) is due to coherency strains at the ledges with the remaining part due to wrong compositional bonds across the inter-

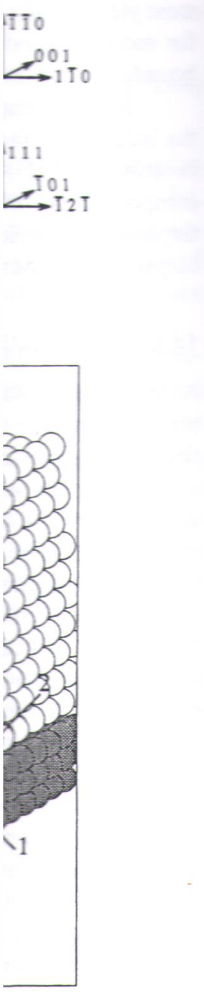

NW orientation rela-
to the close-packed
dislocations in the in-

he chromium con-
ose to the value of
otential above, and
dicate that the ma-
rency strains at the
ds across the inter-

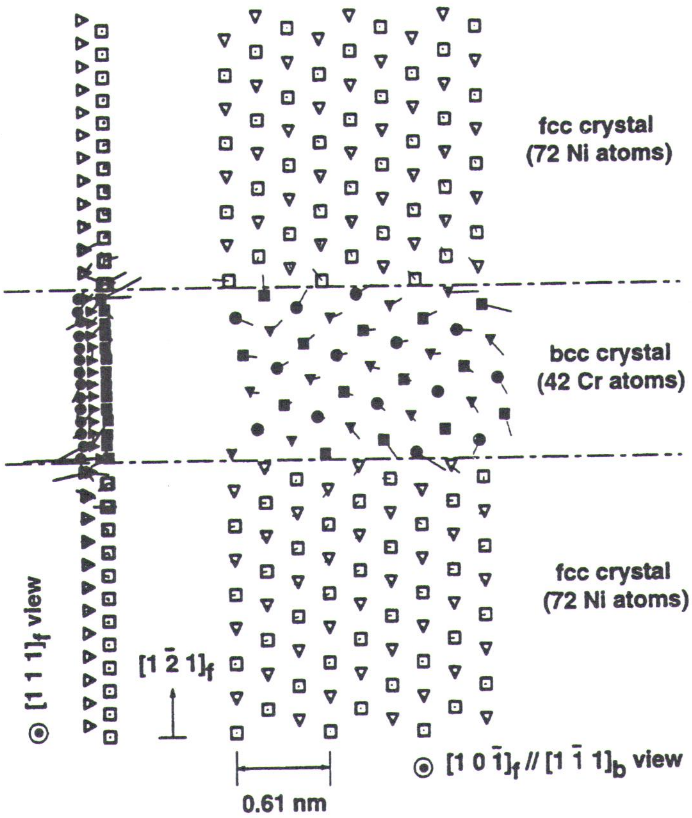

Figure 14.44. Two views of the relaxed structure of a simulation block of the $(121)_{\text{f.c.c.}}$ interface for pure f.c.c. nickel and b.c.c. chromium crystals. Different shapes (squares, triangles and circles) are used to represent atoms on different $(202)_{\text{f.c.c.}}$ and $(222)_{\text{b.c.c.}}$ planes parallel to the paper. The final positions of nickel and chromium atoms are represented by empty and filled shapes, respectively. Relative relaxations indicated by lines attached to the atoms are enlarged 10 times to show their directions. From [102].

face. This type of interface represents the upper limit of coherent interphase boundary energies shown in Table 14.1.

14.7. TERRACE–LEDGE–KINK STRUCTURE OF INTERPHASE BOUNDARIES

When two phases with different compositions but the same crystal structure (Bravais lattice) are separated by a coherent interface, as in the case of the G.P. zone in Figure 12.3, for example, the interface can advance by the replacement of atoms in the α phase on one side of the interface with β atoms by normal lattice diffusion involving vacancies. At temperatures above approximately $0.5T_m$ where significant lattice diffusion occurs, coherent interfaces of this type are relatively diffuse (refer to Figs. 14.3 and 14.5) and there is little barrier to atomic attachment to the interface. Thus, migration is any easy process and is expected to occur as fast as transport of atoms to and away from the interface can occur. This is referred to as diffusion-controlled interfacial motion and the kinetics of this process are described in detail in the following chapter. The same arguments apply if the interface is semicoherent, as in Figure 14.24, provided the misfit dislocations can climb by vacancy creation or annihilation.

A much different situation arises when the two phases forming a coherent or semicoherent interface have different Bravais lattices, particularly if a shear strain e_{ij} is involved in the transformation, as in Eq. (14.46) and Figure 14.39. For example, consider the situation of either of the coherent close-packed interfaces between the f.c.c. and h.c.p. crystals in Figures 12.4 and 14.35. If growth of the h.c.p. phase were to occur by individual atomic attachment randomly on the interface (i.e., by so-called continuous growth, see Sections 5.1 and 10.1), this would require that atoms on *C* sites in the f.c.c. phase at the interface move into *B* positions, as illustrated in Figure 14.45. This is a very unfavorable situation energetically, as it puts two atoms in *B* positions directly across from one another at the interface and it also creates a distortion field around the atom (i.e., it effectively creates a loop of α/6<112> Shockley partial dislocation around the atom). These two effects create a large energy barrier for such an event and promote atoms in the f.c.c. phase to remain in *C* sites at the interface. The same situation is encountered in the coherent regions of semicoherent interfaces separating different phases with different crystal

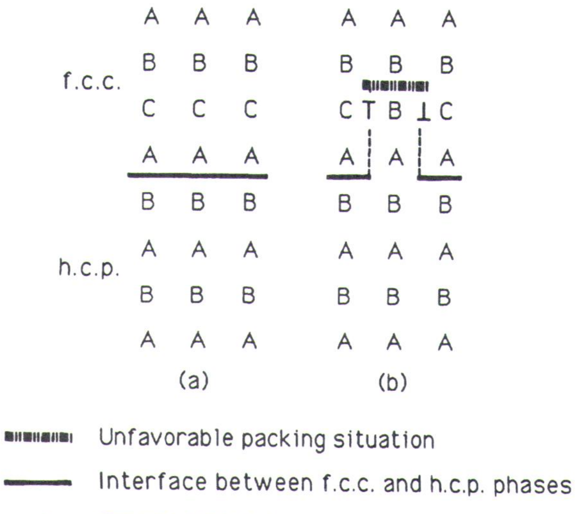

Figure 14.45. Illustration of the difficulties associated with growth of an h.c.p. crystal into an f.c.c. phase by single atom jumps.

structures. This situation is very much analogous to the case of solid–vapor and solid–liquid interfaces, where attachment of single atoms to vicinal surfaces is much more favorable energetically when it occurs at kinks in ledges than on the terraces. In the solid–vapor case, this preferred attachment can be argued by a simple broken-bond model. The same rationale applies to solid–solid interfaces, except that now we must think of wrong compositional bonds across the interface instead of broken bonds. We must also include the strain energy increase indicated by the partial dislocations in Figure 14.45, which requires bond stretching and is very unfavorable energetically. Thus, motion of coherent and semicoherent interfaces between phases with different crystal structures rarely occurs by a continuous growth mechanism.

Migration of these coherent and semicoherent interfaces requires nucleation of ledges that propagate by kinks, just like the vicinal solid–vapor interfaces described in Section 5.2. Thus, the situation is analogous to that of solid–vapor interfaces described in Section 5.2, except that the elastic strain energy associated with nucleation of a pillbox at a solid–solid interface as illustrated for the f.c.c.–h.c.p. interface in Figure 14.45 imposes an additional barrier to nucleation not present at solid surfaces. The strain energy associated with this process is discussed by Christian [1] and is not elaborated further here. With sufficient driving force, ledges nucleate and propagate across heterophase solid–solid interfaces by a terrace–ledge–kink mechanism [23,121] in much the same way as for solid–vapor interfaces.

In the case of solid–solid interfaces, ledges have been found to nucleate by the three mechanisms previously described for solid–vapor interfaces in Section 5.2.1: (a) by dislocations intersecting the interface, (b) by forming vicinal surfaces (e.g., Fig. 12.7) and (c) by two-dimensional nucleation and growth. In the case of precipitates in alloys a variety of other ledge sources have been identified, a common one being particle intersections [159,160]. Unlike the case of two-dimensional nucleation at surfaces, it is difficult to observe nucleation events in solids and two-dimensional nucleation and other mechanisms of nucleation at solid–solid interfaces have not been quantified to the same extent as at solid–vapor interfaces. The formation of kinks in ledges at solid–solid interfaces was studied *in situ* by hot-stage TEM [161] and found to occur by (a) two-dimensional nucleation, (b) deviation of a ledge from a low-energy close-packed direction (i.e., analogous to the vicinal surface as in Fig. 4.2), and (c) intersection of ledges. Thus, the mechanisms and kinetics of kink nucleation at solid–solid interfaces are analogous to those of ledges, which are analogous to those found at solid–vapor interfaces except that elastic strain is often present.

Some of the most convincing evidence for the TLK mechanism of growth of coherent and semicoherent interfaces has come from recent *in situ* hot-stage HRTEM analyses of θ-Al$_2$Cu precipitates in an aluminum–copper–magnesium–silver alloy by Howe et al. [162,163]. These investigators studied the motion of ledges on the faces and at the edges of θ precipitate plates during growth and dissolution in the TEM. Figure 14.46a shows an HRTEM image of a ledge on the face of a θ plate in the α-Al matrix viewed edge-on, parallel to the $\{111\}_\alpha$ habit plane. The $\{111\}_\alpha$ planes appear as bright lines in the right side of the figure and the ledge is two $\{111\}_\alpha$ matrix plane high (one-half of a unit cell of the θ phase). The image shown was photographed during *in situ* growth at about 220°C, and the ledge was observed to oscillate several times per second over a distance of approximately two unit-cells of the θ phase as it moved across the plate face with constant overall velocity in the direction indicated by an arrow. Enhanced atomic motion at the ledge is evidenced by blurring of the image in the region enclosed by a dashed line. Additional *in situ* experiments performed perpendicular to the plate faces (terraces) along a $<111>_{\alpha}$ matrix direction demonstrated that the oscillatory motion of the ledge in Figure 14.46 was caused by the formation and annihilation of kinks along the ledge. One such kink, photographed as it moved along the plate edge, is shown in Figure 14.46b. The kinks are responsible for motion of the ledges both at the edges of the plates and on the plate faces (terraces). They were also found to change their spacing along the edge so that the θ plates could roughen and facet within the habit plane as the temperature was raised and lowered, just like the germanium precipitates shown previously in Figure 14.14. Thus, the terrace–ledge–kink (TLK) model of vicinal surfaces shown in Figure 4.1 applies to coherent and semicoherent solid–solid interfaces when the phases have different crystal structures across the interface.

When ledges, such as the one in Figure 14.46a transform one crystal structure into another, they usually have a dislocation character and an associated strain energy. Thus, any increase in their length increases their energy, and they tend to be relatively straight. This depends only on the lattices of the crystals and is true for interfaces whether or not there is a compositional change across the interface. When there is also a compositional change across the interface, the formation of additional wrong bonds caused by kinks in the ledges provides a second driving force that tends to keep the ledges straight. In f.c.c., h.c.p. and b.c.c. systems, the ledges can often minimize both their elastic and compositional energies by aligning along the close-packed directions in the crystals, and this is observed experimentally. Thus, the orientation relationships discussed in Section 14.6.1 tend to align the close-packed planes and directions between the crystals, and the additional considerations just mentioned further tend to insure that ledges are aligned along the relatively low-index close-packed directions in the interfaces.

In a manner analogous to Figure 14.45, the extra energy associated with perturbing the ledges provides an activation barrier to kink nucleation in solids, and ledges can become immobile in the absence of kinks [121,161]. However, once a kink forms, it is favorable for atoms to attach to it rather than to attach randomly along the ledge, because it does not further increase the length of the ledge or the number of wrong bonds, which is analogous to the solid–vapor situation. It has also been suggested that extra strain associated with kinks helps facilitate substitutional diffusion across the interface at these sites [23]. These concepts apply whether the ledge moves with or without a corresponding compositional change [164].

Another interesting problem that arises in the case of coherent and semicoherent interfaces in solids, which is not a consideration for solid–vapor or solid–liquid interfaces, is how misfit dislocations and structural ledges present at an interface advance to a new terrace as a growing ledge moves across the interface. This situation is depicted for a misfit dislocation in Figure 14.47. Several possible mech-

; photographed dur-
to oscillate several
of the θ phase as it
direction indicated
blurring of the in-
eriments performed
x direction demon-
s caused by the fin-
, photographed as it
s are responsible for
ate faces (terraces).
at the θ plates could
raised and lowered,
14.14. Thus, the ter-
re 4.1 applies to in-
have different crys-

ne crystal structure
sociated strain ener-
they tend to be rel-
and is true for inter-
he interface. When
mation of addition-
d driving force that
ems, the ledges can
aligning along the
xperimentally. Thus,
to align the close-
ional considerations
along the relatively

associated with per-
ation in solids, and
]. However, once a
to attach randomly
of the ledge or the
situation. It has also
ilitate substitutional
s apply whether the
nge [164].
herent and semico-
-vapor or solid–liq-
present at an inter-
s the interface. This
veral possible mech-

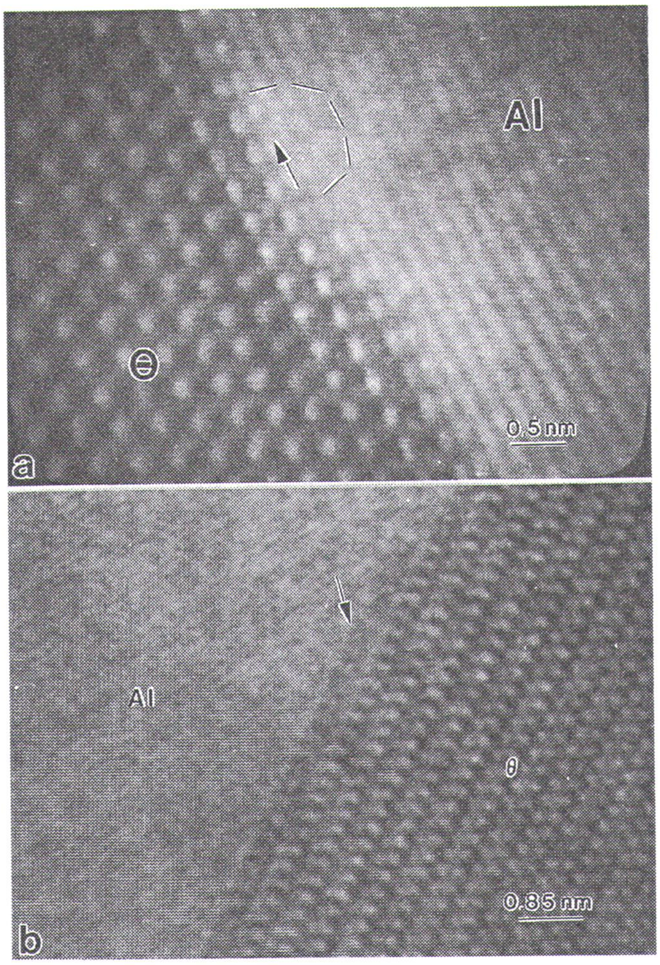

Figure 14.46. HRTEM images of (a) a ledge and (b) a kink on a θ plate during *in situ* growth in the TEM. From [162,163].

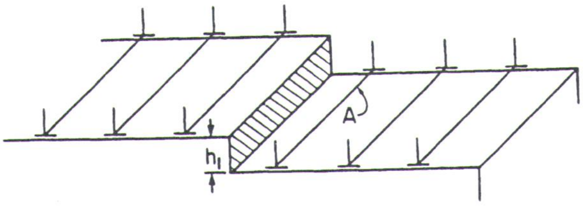

Figure 14.47. Illustration of ledge growth (with height h_l) to the right along a terrace containing misfit dislocations. Dislocation *A* is closest to the advancing ledge. Reprinted with permission from [165] by Elsevier Science Ltd., Oxford, England.

anisms have been proposed, such as climb of the misfit dislocations up the ledges, glide of the misfit dislocations along the terraces in front of the ledge, and so forth [165]. There is experimental evidence for some of the proposed mechanisms [154, 166], but this area has not been thoroughly explored.

PROBLEMS

14.1. Why might Eq. (14.1) not be applicable when the phases across a coherent interphase boundary have different crystal structures?

14.2. (a) Use Eq. (14.16) together with Eq. (14.11) to plot the interfacial energy γ_{cR}^{SS} of an aluminum–zinc alloy with composition $X_{Zn} = 0.4$ from 25°C to the critical temperature $T_c = 351.5$°C. The aluminum–zinc phase diagram is shown in Problem 2.8.

(b) Make three sketches of the interface profile for the aluminum–zinc system at $T = 0$ K, $T_c/5$ and T_c. Explain the physical basis of these sketches.

14.3. The interfacial energy for a coherent interface γ_c^{SS} was calculated for a gold–50 at.% nickel alloy at 400°C in Section 14.2.1. Repeat the calculations for gold–copper and gold–platinum alloys under the same conditions and explain any trends in your results.

14.4. On the same figure, sketch the interface profiles for two different regular solution alloys (*A* and *B*) with the same solute content X_c at the same temperature $T_c/5$, where the regular solution parameter of the solid phase Ω^S is significantly greater in alloy *A* than in alloy *B*.

14.5. Using Eq. (4.3) and the data in Table 1 in the article by Cahn and Hilliard [*J. Chem. Phys.*, **28,** 258 (1958)], plot $\gamma_{cR}^{2/3}$ versus *T* for neon, argon, nitrogen and oxygen. Compare the results and explain any trends.

14.6. Show that the partial molar free energy of each species in an *A–B* alloy is the same everywhere within the interphase boundary region, where the composition varies rapidly with distance normal to the interface. You may use either the continuum or DLP approach.

14.7. Explain why fully coherent precipitates with a small misfit tend to loose coherency as they grow.

14.8. The figure below (from [113]) shows a [010] projection of two ordered domains of $L1_2$ phase with (001), (100) and (110) APBs. Determine whether each boundary is conservative or nonconservative and explain your reasoning. X indicates sites preferentially occupied by minority species. Large and small circles indicate, respectively, atomic sites on alternate planes with differing elevations.

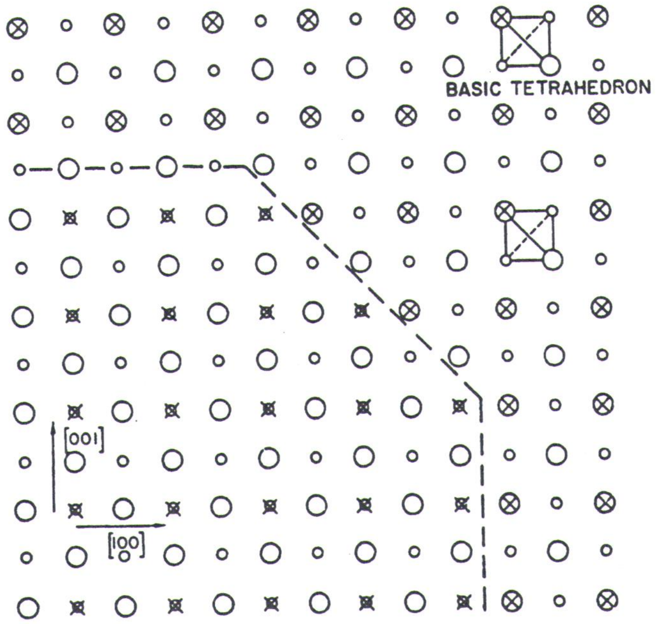

14.9. Use Eq. (14.30) to calculate the APB energy on the {111} planes in the $L1_2$ structures Cu_3Au and Cu_3Pt. Explain any difference in the energies based on nearest-neighbor bonding.

14.10. Calculate the APB energy γ_{apb} on the {111} plane in Cu_3Au and compare it with the {111} interphase boundary energy γ_c^{SS} between copper- and gold-rich phases, assuming negligible solid solubility in each phase.

14.11. Explain the structures and energies of coherent, semicoherent and incoherent interfaces with particular reference to the role of orientation relationships and misfit.

14.12. Consider a {110} interphase boundary formed between two identically oriented b.c.c. crystals that differ in composition and lattice parameter.

(a) Determine the geometry of the misfit dislocation array for dislocations with an $a/2\langle 111\rangle$ Burgers vector. Repeat for dislocations with an $a\langle 100\rangle$ Burgers vector.

(b) Calculate the relative structural interfacial energy γ_s^{SS} of these two dislocation arrays, assuming that the energy is proportional to the square of the magnitude of the Burgers vector.

(c) Which dislocation array is more likely to appear on the basis of minimum interfacial energy?

(d) Under what conditions will the chemical component of the interphase boundary energy of these two interfaces become of minor importance relative to the structural component?

14.13. A 20-nm-thick film of pure silicon is deposited on a (100) Ge_xSi_{1-x} substrate where the lattice mismatch is 1.9%.

(a) The lattice parameters of silicon and germanium are 0.543 nm and 0.566 nm, respectively. What is the value of x in Ge_xSi_{1-x}?

(b) Dislocations are formed with Burgers vectors **b** oriented along the <110> directions. For silicon, Poisson's ratio is 0.272 and the shear modulus is 0.67×10^{11} N/m^2. Assume the elastic stress field of the misfit dislocations extends 20 nm (the film thickness). Find the magnitude of the Burgers vector b and the spacing of the misfit dislocations D_δ.

(c) Calculate the interfacial energy γ_s^{SS} of an array of noninteracting edge dislocations with Burgers vector **b**.

14.14. Consider a film of f.c.c. copper ($a = 0.3615$ nm) on a gold substrate ($a = 0.4079$ nm), where the film is relaxed by misfit dislocations.

(a) Assume the interface plane is (111). If the misfit dislocations lie on the (111) plane in the <110> directions, what is the magnitude of the Burgers vector and the spacing of the dislocations?

(b) Assume the interface plane is (100). If the misfit dislocations lie on the (111) plane in the <110> directions, what is the magnitude of the Burgers vector and the spacing of the dislocations?

14.15. Derive Eq. (14.42).

14.16. A weak-beam dark-field TEM image of misfit dislocations between islands of gallium antimonide sitting on a gallium arsenide substrate is shown below (from [167]). The dislocations (white lines) are parallel to <110> directions in the crystals.

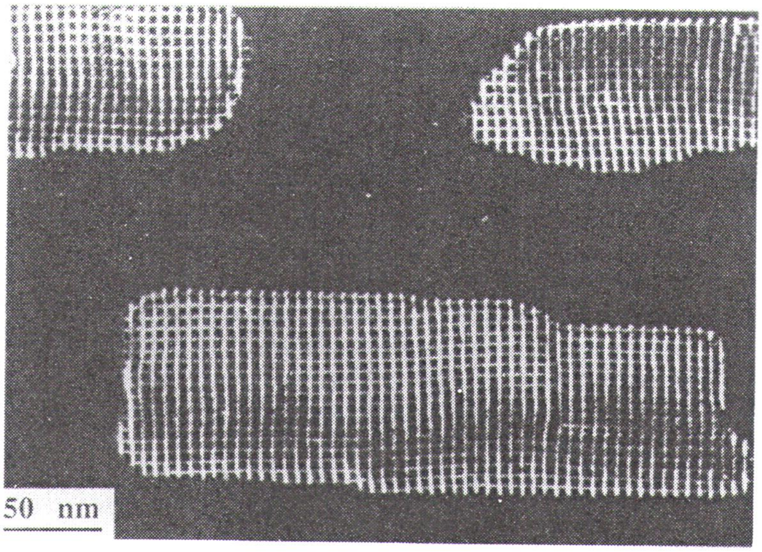

(a) Calculate the misfit across the interface assuming that the dislocations have Burgers vectors **b** = $\alpha/2\langle 110\rangle$.

(b) Compare the misfit in part (a) with that calculated using the lattice parameters of gallium antimonide and gallium arsenide and provide an explanation for any differences in the values.

14.17. A Burgers circuit drawn around an interfacial dislocation at an annealed CdTe/GaAs interface in a <110> HRTEM image is shown below (from [14]). Determine the Burgers vector of the dislocation.

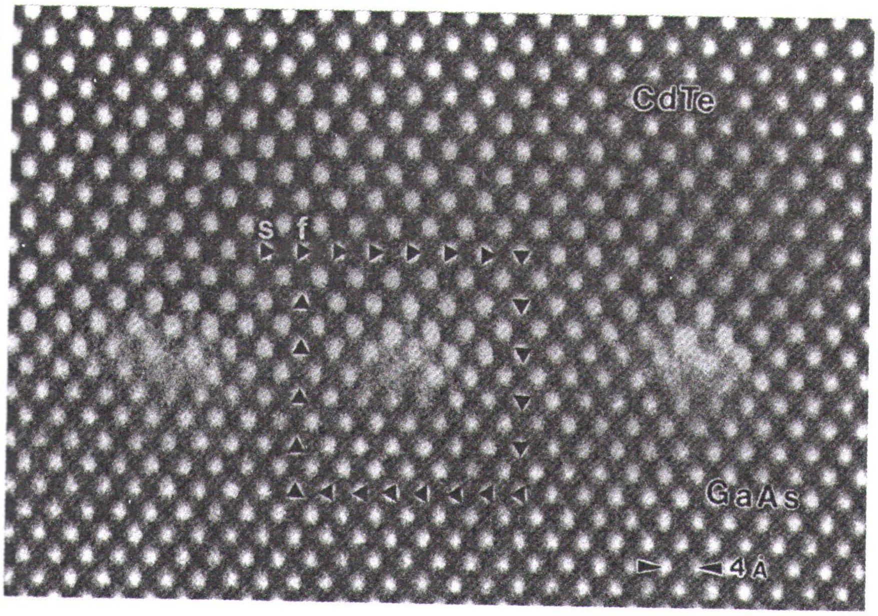

14.18. (a) Make a sketch similar to Figure 7.10 to illustrate the atomic matching between the close-packed planes of b.c.c. and h.c.p. crystals when their close-packed directions are aligned.

(b) What lattice parameter ratio ($\alpha_{\text{b.c.c.}}/\alpha_{\text{h.c.p.}}$) would produce exact coincidence of the atoms along the close-packed directions in the two crystals?

14.19. The transformation in Figures 7.10 and 14.36 can be represented by a transformation matrix **A** that consists of a deformation **S** as in Eq. (14.45) and a rigid body rotation **R** given by

$$\mathbf{R} = \begin{bmatrix} \cos\theta & -\sin\theta \\ \sin\theta & \cos\theta \end{bmatrix}$$

as in Section 13.2.2, such that **A** = **RS**. Using these matrices, show that Dahmen's invariant line is equivalent to an O-line.

(14.47) and (14.49),
$e_{11} = 0.1$ and $e_{12} =$

als is shown below
orientation relation-
icated on the figure.

DSC lattice as the

.c. and h.c.p. crystal

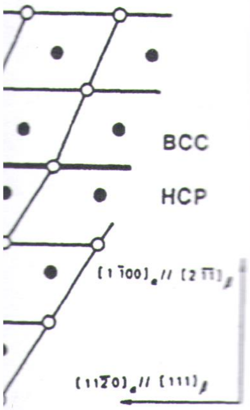

dge is shown below
he two lattices is

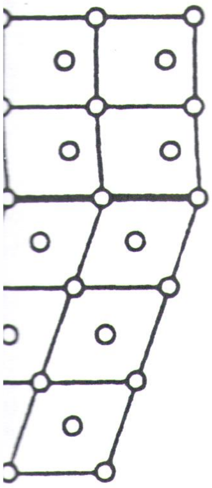

(a) Construct the DSC lattice for the interface.

(b) Determine the Burgers vector of the ledge using the DSC lattice as the reference lattice.

(c) Specify the Burgers vector of the ledge with reference to the b.c.c. and h.c.p. phases.

14.23. An enlargement of several ledges in Figure 12.7 is shown below. The orientation of the crystals in the image is $[0\bar{1}1]_{\gamma} \| [1\bar{1}1]_{B2}$ with the parallel close-packed planes forming the terraces of the ledged interface. Construct the DSC lattice for this interface and determine the ledge–dislocation character of the ledges. The γ phase can be assumed to be f.c.c., the B2 phase is b.c.c. and the crystals have the Burgers orientation relationship given in Eq. (14.44b).